Spectral Energy Landscapes, Multiscale Window Entropies, and Continuous Bubble Relaxation of Magic Squares

Kyle Elliott Mathewson
Faculty of Science, University of Alberta
kyle.mathewson@ualberta.ca

Abstract

Every magic square of order n is a zero-energy ground state of the line-indicator Hamiltonian $\mathcal{H}_{\text{line}}(S) = \sum_{L\in\mathcal{L}_n} R_L(S)^2 = \mathbf{z}^\top L_n \mathbf{z}$ on the symmetric group S_{n^2}, where $\mathbf{z} \in \mathbb{R}^{n^2}$ is the centred height field $Z_{ij} = 2s_{ij} - (n^2+1)$ and $L_n = A_n^\top A_n$ is the $(2n+2)$-line incidence Laplacian. While previous papers in this series established the convex-polytopal geometry of Magic Gems (Paper I), their universal bivariate polynomial moments and isotropic inertia tensors (Paper II), and their rigid-body Euler–Poinsot rotational mechanics (Paper III), a fundamental inverse question remained open: how does the combinatorial energy landscape $\mathcal{H}_{\text{line}} : S_{n^2} \to \mathbb{Z}_{\geq 0}$ organize the $n^2!$ permutations around the magic ground-state manifold, why do standard continuous and single-particle physical relaxation dynamics fail to find it, and what multiscale physical mechanisms succeed? Here we resolve this question across four scales. First, we prove the *Spectral Rationalization Theorem*: although L_n on $\mathbb{R}^{n^2}$ possesses irrational eigenvalues $\lambda_\pm(n)$ arising from row–column–diagonal overlap, restricting L_n to the (n^2-1)-dimensional zero-mean hyperplane $\mathbf{1}^\perp$ inhabited by all centred permutations decouples the constant mode and collapses the entire spectrum into exact integers—$\{0^{[n^2-2n-1]}, (n-2)^{[1]}, n^{[2n-1]}\}$ for even $n \geq 4$ and $\{0^{[n^2-2n-1]}, (n-1)^{[2]}, n^{[2n-2]}\}$ for odd $n \geq 3$—with a universal mean eigenvalue $\bar{\mu}(\widetilde{L}_n) = 2$ and exact random-permutation ensemble expectation $\mathbb{E}[\mathcal{H}_{\text{line}}(S)] = 2\|\mathbf{z}\|^2 = \frac{2}{3}n^2(n^4-1)$. We also prove a *Low-Mode Insufficiency Proposition*, constructing an explicit 4×4 counterexample S_{low} whose macroscopic dipole moments $\langle X, Z\rangle = \langle Y, Z\rangle = 0$ and main diagonals $R_{D_\pm} = 0$ vanish identically, yet which remains trapped at $\mathcal{H}_{\text{line}}(S_{\text{low}}) = 1{,}584 > 0$ inside the $(2n-4)$-dimensional zero-mean "optical phonon" subspace of $\text{im}(\widetilde{L}_n)$ ($2n-3$ in $\text{im}(L_n)$). Second, we introduce multiscale sliding-window energies and Shannon entropies $H_p(k)$ across all 880 Frénicle order-4 magic squares and constructive families at $n \in \{3,4,5,6,8\}$, proving that vanishing interior 2×2 quartet energy ($W^{\text{int}}_{2\times 2} = 0$) is equivalent on even-order magic squares ($n = 2m$) to vanishing toroidal quartet energy ($W^{\text{tor}}_{2\times 2} = 0$) and isolates the 48 panmagic squares of Dudeney Group I at $n = 4$, while the Concentric Shell Quadrupole Identity $M_{xyz}(S) = -8\,Q_{\text{corner}}(S) - 3\,Q_{\text{edge}}(S)$ proves that the mixed octupole moment vanishes on all 48 Group III associative squares plus exactly 8 coprime-resonance squares (4 each in Groups IX and X). Third, we derive the exact quadratic transposition law $\Delta\mathcal{H}_{\text{line}}(\tau_{ab}) = -2d(g_a - g_b) + c_{ab}d^2$ ($c_{ab} \in \{2,\ldots,7\}$) and perform an exhaustive census of all $9! = 362{,}880$ states of S_9, discovering that $n = 3$ possesses *exactly* 8 *spurious strict local minima* forming a single dihedral orbit $S^{(3)}_{\text{trap}}$ at $\mathcal{H}_{\text{line}} = 8$ that traps 25.47% of S_9 under both Kawasaki 2-body spin exchange and Zener 3-body ring diffusion, yet escapes across an intermediate single-swap saddle ($\mathcal{H}^\ddagger_{\text{line}} = 12, \Delta\mathcal{H}^\ddagger_{\text{line}} = +4$) via a *unique* Pauling spin-ice divergence-free $(2,2)$ loop update $(6 \leftrightarrow 7)(3 \leftrightarrow 4)$ (1 of 378 disjoint double swaps) that restores the deterministic ground-state basin of S_9 to 362,880/362,880 (100.00%). Fourth, we systematically contrast failed physical relaxation analogs (macroscopic torque relaxation, overdamped colloidal drift under both greedy snapping and exact Hungarian bipartite matching at 0.0%, Kawasaki 2-spin quench at 20.0%, and Zener 3-ring thermal annealing at 32.5%) against a *Re-Anchored Hierarchical Multi-Cycle Settler* uniting spin-ice $(2,2)$ loop moves, 4-body quadrupolar swaps, crystallographic slip-plane glide, and Wales–Doye / chaperonin re-anchored basin-hopping to achieve 100.0% *ground-state synthesis across all orders* $n = 3,4,5,6,7,8$ (up to $64! \approx 1.27\times 10^{89}$ states), analyzed via the Maxwell–Calladine floppy-to-constraint ratio $\eta_{\text{MC}}(n) = (n^2-2n-1)/(2n)$ and the $1 - 2/(n-1)^2$ diagonal-free $(2,2)$ subspace fraction.

1 Introduction

A magic square of order n is a bijection $S : \{1, \dots, n\}^2 \to \{1, \dots, n^2\}$ whose n rows, n columns, and two main diagonals each sum to the magic constant $M_n = \frac{1}{2}n(n^2+1)$ [10, 6, 8, 1]. When lifted into three-dimensional Euclidean space via centred integer coordinates

$$X_j = 2j - (n+1), \qquad Y_i = (n+1) - 2i, \qquad Z_{ij} = 2s_{ij} - (n^2+1), \tag{1}$$

each permutation $S \in S_{n^2}$ defines an n^2-point configuration $\mathcal{P}(S) = \{(X_j, Y_i, Z_{ij})\} \subset \mathbb{Z}^3$ whose convex hull $K(S) = \operatorname{conv} \mathcal{P}(S)$ is a *Magic Gem*. Across the first three papers of this series, we investigated the forward map from magic squares to geometric and mechanical invariants:

1. **Paper I (*Polytopal Geometry*)** [15] classified the facial structure, vertex counts V, surface areas, volumes, and discrete symmetry groups of Magic Gems across the 880 Frénicle order-4 squares and higher-order families.

2. **Paper II (*Bivariate Moments & Orthogonality*)** [14] proved that semi-magic balance forces $\langle X^j, Z\rangle = \langle Y^j, Z\rangle = 0$ for all $j \geq 0$, diagonalizing the 3×3 inertia and covariance tensors of every magic square and generating universal Prouhet–Tarry–Escott power-sum identities.

3. **Paper III (*Rigid-Body Mechanics & Structural Stability*)** [13] tested these algebraic invariants in physical rigid-body mechanics, proving that every equal-vertex-mass Magic Gem is an oblate symmetric top ($I_{xx} = I_{yy} < I_{zz}$) free of intermediate-axis Dzhanibekov tumbling, while continuous bulk polyhedra break covariance isotropy yet preserve exact static stability across all 50,334 facets of the 880 order-4 gems.

Despite this complete characterization of the *ground states*, a central statistical-mechanical and algorithmic question remained open: *how are the magic ground states embedded within the ambient $n^2!$-state permutation space S_{n^2}, and what physical or combinatorial dynamics can relax an arbitrary disordered permutation into a magic square?* Treating magic square synthesis as energy minimization on a frustrated discrete lattice connects classical combinatorics to spin-glass theory [18], rugged potential energy landscapes [24], and stochastic annealing [12]. In an interactive companion laboratory (`physicalSolver` [16]), we prototyped four complementary physical representations of this inverse problem: a spectral operator decomposition of line residuals, a multiscale sliding-window entropy analyzer, a discrete permutation-cycle descent engine, and a continuous "Bubble Trinity" Langevin particle simulator.

Following Whitesides's blueprint-driven methodology for connecting mathematical structure to quantitative experiments [27], this fourth paper formalizes the mathematical operators underlying `physicalSolver` and establishes exact theorems and exhaustive computational censuses for each stage of the relaxation hierarchy. Let $\mathcal{L}_n$ denote the set of $2n+2$ magic lines (n rows, n columns, and 2 main diagonals), and let $R_L(S) = \sum_{(i,j)\in L} Z_{ij}$ be the centred residual of line $L \in \mathcal{L}_n$. Collecting the $2n+2$ line indicator vectors as rows of the incidence matrix $A_n \in \{0,1\}^{(2n+2)\times n^2}$, the *line-indicator Hamiltonian* takes the quadratic form

$$\mathcal{H}_{\text{line}}(S) = \sum_{L\in\mathcal{L}_n} R_L(S)^2 = \|A_n \mathbf{z}\|_2^2 = \mathbf{z}^\top L_n \mathbf{z}, \qquad L_n = A_n^\top A_n \in \mathbb{Z}^{n^2\times n^2}. \tag{2}$$

By construction, $\mathcal{H}_{\text{line}}(S) \geq 0$ for all $S \in S_{n^2}$, and $\mathcal{H}_{\text{line}}(S) = 0$ if and only if S is a magic square.

Summary of Main Results

Our investigation proceeds from global linear operators on $\mathbb{R}^{n^2}$ to local multiscale sub-windows, discrete swap-graph topology on S_{n^2}, and continuous Langevin relaxation (Table 1):

Table 1: Overview of the four-scale physical solver hierarchy and principal theorems established in Paper D.

Scale / Section	Operator / Observable	Exact Theorem / Census	Key Quantitative Invariant
Sec. 2: Spectral Operator on $\mathbf{1}^\perp$	Line Laplacian $L_n = A_n^\top A_n$ Random ensemble $\mathbb{E}[\mathcal{H}_{\text{line}}]$ Dipole + diag energy E_{low}	Theorem 2.1 ($\mathbf{1}^\perp$ rationalization) Theorem 2.2 (universal mean $\bar{\mu} = 2$) Proposition 2.3 ($2n-4$ optical modes)	$\text{spec}(\widetilde{L}_n) \subset \mathbb{Z}$, $\ker = n^2 - 2n - 1$ $\mathbb{E}[\mathcal{H}_{\text{line}}] = 2\|\mathbf{z}\|^2 = \frac{2}{3}n^2(n^4-1)$ S_{low}: $E_{\text{low}} = 0$, $\mathcal{H}_{\text{line}} = 1{,}584$
Sec. 3: Multiscale Windows & Parity	2×2 quartet energy $W_{2\times 2}$ Shell quadrupoles $Q_{\text{corner}}, Q_{\text{edge}}$ Window entropy $\widetilde{H}_p(k)$	Theorem 3.1 (interior $\Leftrightarrow$ toroidal) Proposition 3.2 ($M_{xyz} = -8Q_{\text{corner}} - 3Q_{\text{edge}}$) Constructive census ($n = 3\ldots 8$)	$W^{\text{int}}_{2\times 2} = 0 \iff$ Group I (48/880) $M_{xyz} = 0$ on 48 Grp III +8 Grp IX/X Max $\widetilde{H}_1(2) = 0.99967$ (#123, Grp VI)
Sec. 4: Swap Landscape on S_{n^2}	Transposition cost $\Delta\mathcal{H}_{\text{line}}(\tau_{ab})$ S_9 exhaustive basin census S_{16} descent (2,000 starts)	Proposition 4.1 (exact quadratic law) Theorem 4.2 (8 traps $S^{(3)}_{\text{trap}}$, $\Delta\mathcal{H}^{\ddagger}_{\text{line}} = +4$) Order-4 local-minimum spectrum	$\Delta\mathcal{H}_{\text{line}} = -2d(g_a - g_b) + c_{ab}d^2$ ($c_{ab} \le 7$) 74.53% $\to$ 100.00% w/ unique $(2,2)$ 18.25% (2-cycle) $\to$ 25.45% w/ $(2,2)$
Sec. 5: Continuous Bubble Relaxation	Bubble-Trinity Langevin SDE Re-anchored hierarchical settler	Regimes I–IV (greedy & Hungarian) 7-tier ablation & multi-order ($n = 3\ldots 8$)	$\mathcal{H}_{\text{ind}}$: 1681.9 $\to$ 1050.6 (Regime IV) 100.0% synthesis across all $n = 3\ldots 8$

1. **Spectral Rationalization & Low-Mode Insufficiency (Section 2):** In Theorem 2.1, we prove that while the unprojected Laplacian L_n on $\mathbb{R}^{n^2}$ has irrational eigenvalues $\lambda_\pm(n)$ caused by the coupling between the constant vector $\mathbf{1}$ and the two main diagonals, restricting L_n to the zero-mean hyperplane $\mathbf{1}^\perp$ via $\widetilde{L}_n = P_{\mathbf{1}^\perp} L_n P_{\mathbf{1}^\perp}$ collapses all eigenvalues into exact integers: $\{0^{[n^2-2n-1]}, (n-2)^{[1]}, n^{[2n-1]}\}$ for even $n \ge 4$ and $\{0^{[n^2-2n-1]}, (n-1)^{[2]}, n^{[2n-2]}\}$ for odd $n \ge 3$. In Theorem 2.2, we prove directly from the trace identity $\text{tr}(\widetilde{L}_n) = \text{tr}(L_n) - \hat{\mathbf{1}}^\top L_n \hat{\mathbf{1}} = (2n^2+2n) - (2n+2) = 2(n^2-1)$ that the mean eigenvalue of $\widetilde{L}_n$ on $\mathbf{1}^\perp$ is *identically* 2 for all $n \ge 3$, yielding the exact random-permutation expectation $\mathbb{E}[\mathcal{H}_{\text{line}}(S)] = 2\|\mathbf{z}\|^2 = \frac{2}{3}n^2(n^4-1)$ (Figure 1a). In Proposition 2.3, we prove that enforcing Paper II's dipole orthogonality $\langle X, Z\rangle = \langle Y, Z\rangle = 0$ together with diagonal balance $R_{D_+} = R_{D_-} = 0$ constrains only a 4-dimensional subspace of the $2n$-dimensional zero-mean active image $\text{im}(\widetilde{L}_n) \subset \mathbf{1}^\perp$, leaving a $(2n-4)$-dimensional zero-mean "optical phonon" residual subspace ($2n-3$ in $\text{im}(L_n)$) exemplified at $n = 4$ by an explicit permutation S_{low} with $\mathcal{H}_{\text{line}}(S_{\text{low}}) = 1{,}584$ (Figure 1b).

2. **Multiscale Window Entropies, Quartet Equivalence, and Shell Quadrupoles (Section 3):** Moving beyond 1D line sums to 2D local patches, we analyze sliding $k \times k$ sub-window energies and normalized Shannon entropies $\widetilde{H}_p(k)$ across constructive families ($n = 3, 4, 5, 6, 8$) and all 880 order-4 squares (Figure 2). In Theorem 3.1, we prove that for any even-order magic square ($n = 2m$), vanishing of the $(2m-1)^2$ interior 2×2 quartet sums ($W^{\text{int}}_{2\times 2}(S) = 0$) automatically forces all $4m^2 - (2m-1)^2$ boundary-wrapping toroidal 2×2 quartets to vanish ($W^{\text{tor}}_{2\times 2}(S) = 0$), isolating the 48 panmagic squares of Dudeney Group I at $n = 4$. In Proposition 3.2, we prove the Concentric Shell Quadrupole Identity $M_{xyz}(S) = -8\,Q_{\text{corner}}(S) - 3\,Q_{\text{edge}}(S)$, showing why $B_{\text{comp}}(S) \in \{0, 8\}$ is binary across all 880 squares and why $M_{xyz}(S)$ vanishes on all 48 Group III associative squares plus exactly 8 coprime-resonance squares in Groups IX and X (Figure 3).

3. **Combinatorial Swap Landscape, Antipodal Traps & Unique $(2,2)$ Escape (Section 4):** In Proposition 4.1, we derive the exact closed-form energy change $\Delta\mathcal{H}_{\text{line}}(\tau_{ab}) = -2d(g_a - g_b) + c_{ab}d^2$ ($c_{ab} \in \{2, \ldots, 7\}$) under any 2-cycle transposition τ_{ab}. Exhaustive evaluation across all $9! = 362{,}880$ permutations of S_9 (Theorem 4.2 and Figure 4) reveals a striking topological obstruction: besides the 8 Lo Shu ground states ($\mathcal{H}_{\text{line}} = 0$), S_9 contains *exactly* 8 *spurious strict local minima* forming a single D_4 orbit $S^{(3)}_{\text{trap}}$ at $\mathcal{H}_{\text{line}} = 8$ ($E_{\text{std}} = 2$). Every single 2-cycle ($\min \Delta\mathcal{H}_{\text{line}} = +4$) AND every single 3-cycle ($\min \Delta\mathcal{H}_{\text{line}} = +8$) on $S^{(3)}_{\text{trap}}$ strictly increases $\mathcal{H}_{\text{line}}$. However, testing all $\frac{1}{2}\binom{9}{2}\binom{7}{2} = 378$ disjoint $(2,2)$ double transpositions proves that *one and only one*—the row-preserving double swap $(6 \leftrightarrow 7)(3 \leftrightarrow 4)$, which traverses an intermediate single-swap saddle at $\mathcal{H}^{\ddagger}_{\text{line}} = 12$ ($\Delta\mathcal{H}^{\ddagger}_{\text{line}} = +4$)—escapes $S^{(3)}_{\text{trap}}$ directly to the Lo Shu ground state, expanding the deterministic ground-state basin of S_9 from 270,442/362,880 (74.53%) to 362,880/362,880 (100.00%). At order $n = 4$ (S_{16}), line-preserving $(2,2)$ double swaps escape 16.57% of trapped 2-cycle local minima (4.83× more than 3-cycles at 3.43%), raising deterministic steepest-descent convergence from 18.25% to 25.45% (Figure 5).

4. **Continuous "Bubble Trinity" Relaxation, Physical Mechanism Ablation & 100% Multi-Order Settling (Section 5):** Finally, we embed the discrete grid into $\mathbb{R}^2$ by treating the n^2 integers as mobile viscoelastic "bubbles" coupled to home lattice wells, pairwise core repulsion, and a continuous line-residual force field (Figure 6a). We systematically contrast why naive physical relaxation mechanisms fail—including macroscopic torque balance (blind to the $2n-3$ optical phonon modes), overdamped colloidal drift with greedy lattice snapping (0.0% convergence due to hard-core boundary eviction cascades), Kawasaki 2-body spin exchange (20.0% at $n=4$, 1.0% at $n=5$), and Zener 3-ring vacancy annealing (32.5% at $n=4$, 0.0% at $n=5$)—against the cooperative multiscale mechanisms that succeed (Figure 6b, Table 7). Combining $O(1)$ Kawasaki 2-cycle steepest descent, crystallographic slip-plane glide (whole-row/column permutations), Pauling spin-ice divergence-free $(2,2)$ loop moves, Weaire–Rivier $T1$ / Falk–Langer Eshelby quadrupolar $(2,2)$ rearrangements, and Wales–Doye / GroEL chaperonin re-anchored basin-hopping yields a *Re-Anchored Hierarchical Multi-Cycle Settler* (Table 8) that achieves 100.0% **ground-state synthesis across all orders** $n=3,4,5,6,7,8$ (up to $64! \approx 1.27\times10^{89}$ states) and reveals a *Maxwell–Calladine Floppy-Mode Dimensional Relief Phenomenon* governed by the floppy-to-constraint ratio $\eta_{\mathrm{MC}}(n) = (n^2-2n-1)/(2n)$ (Figure 7).

2 Spectral Rationalization of the Line-Incidence Laplacian

To analyze the global geometry of the line-indicator Hamiltonian $\mathcal{H}_{\mathrm{line}}(S) = \mathbf{z}^\top L_n \mathbf{z}$ defined in Equation 2, we first determine the exact spectral decomposition of the line-incidence Laplacian $L_n = A_n^\top A_n$ both on the ambient Euclidean space $\mathbb{R}^{n^2}$ and on the zero-mean hyperplane $\mathbf{1}^\perp = \{\mathbf{z}\in\mathbb{R}^{n^2} : \mathbf{1}^\top\mathbf{z}=0\}$ where every centred permutation vector $\mathbf{z}(S)$ resides.

2.1 Incidence Structure and Spectral Rationalization on $\mathbf{1}^\perp$

Let $\mathbf{r}_1,\dots,\mathbf{r}_n \in \{0,1\}^{n^2}$ denote the row-indicator vectors of the $n\times n$ grid, $\mathbf{c}_1,\dots,\mathbf{c}_n \in \{0,1\}^{n^2}$ the column-indicator vectors, and $\mathbf{d}_+,\mathbf{d}_- \in \{0,1\}^{n^2}$ the main and anti-diagonal indicator vectors. Then

$$L_n = A_n^\top A_n = \sum_{i=1}^{n} \mathbf{r}_i\mathbf{r}_i^\top + \sum_{j=1}^{n} \mathbf{c}_j\mathbf{c}_j^\top + \mathbf{d}_+\mathbf{d}_+^\top + \mathbf{d}_-\mathbf{d}_-^\top. \tag{3}$$

Because the n rows partition the n^2 cells and the n columns also partition the n^2 cells, $\sum_{i=1}^n \mathbf{r}_i = \sum_{j=1}^n \mathbf{c}_j = \mathbf{1}_{n^2}$. This single linear dependency reduces the rank of the $2n$ row and column indicators from $2n$ to $2n-1$. Since the two main diagonals $\mathbf{d}_+$ and $\mathbf{d}_-$ are linearly independent of the row and column span for all $n\geq 3$, $\operatorname{rank}(A_n) = 2n+1$. However, because $\mathbf{d}_+$ and $\mathbf{d}_-$ have non-zero inner product $\mathbf{1}^\top\mathbf{d}_\pm = n$ with the constant vector $\mathbf{1}$ (and intersect at the central cell when n is odd, $\mathbf{d}_+^\top\mathbf{d}_- = 1$, or are disjoint when n is even, $\mathbf{d}_+^\top\mathbf{d}_- = 0$), the unprojected operator L_n on $\mathbb{R}^{n^2}$ mixes the constant mode $\mathbf{1}$ with the symmetric diagonal mode $\mathbf{d}_+ + \mathbf{d}_-$, producing irrational eigenvalues. Restricting to $\mathbf{1}^\perp$ eliminates this coupling completely:

Theorem 2.1 (Spectral Rationalization of the Line-Incidence Laplacian)**.** *For every order $n\geq 3$, the line-incidence matrix $A_n \in \{0,1\}^{(2n+2)\times n^2}$ has rank $2n+1$, and the magic nullspace $\ker(L_n) = \ker(A_n)$ has dimension*

$$\dim\ker(L_n) = n^2 - 2n - 1, \tag{4}$$

all of whose basis vectors lie in the zero-mean hyperplane $\mathbf{1}^\perp$. Furthermore:

1. ***Unprojected Spectrum on $\mathbb{R}^{n^2}$:** The $2n+1$ non-zero eigenvalues of L_n on $\mathbb{R}^{n^2}$ consist of two irrational roots $\lambda_\pm(n)$ together with integer eigenvalues:*

$$\operatorname{spec}(L_n) = \begin{cases} \left\{0^{[n^2-2n-1]},\ \lambda_-(n)^{[1]},\ n^{[2n-1]},\ \lambda_+(n)^{[1]}\right\}, & \text{even } n\geq 4, \\ \left\{0^{[n^2-2n-1]},\ \lambda_-(n)^{[1]},\ (n-1)^{[1]},\ n^{[2n-2]},\ \lambda_+(n)^{[1]}\right\}, & \text{odd } n\geq 3, \end{cases} \tag{5}$$

where $\lambda_\pm(n) = \frac{1}{2}\big(3n \pm \sqrt{n(n+16)}\big)$ *for even* n *and* $\lambda_\pm(n) = \frac{1}{2}\big(3n+1 \pm \sqrt{n^2+14n+1}\big)$ *for odd* n.

2. ***Rationalized Zero-Mean Spectrum on*** $\mathbf{1}^\perp$***:*** *Let* $P_{\mathbf{1}^\perp} = I_{n^2} - \frac{1}{n^2}\mathbf{1}\mathbf{1}^\top$ *denote the orthogonal projector onto* $\mathbf{1}^\perp$*, and let* $\widetilde{L}_n = P_{\mathbf{1}^\perp} L_n P_{\mathbf{1}^\perp}\big|_{\mathbf{1}^\perp}$ *be the restricted Laplacian on the* (n^2-1)*-dimensional zero-mean subspace. On* $\mathbf{1}^\perp$*, the irrational roots* $\lambda_\pm(n)$ *collapse into exact integers:*

$$\operatorname{spec}\big(\widetilde{L}_n\big|_{\mathbf{1}^\perp}\big) = \begin{cases} \Big\{0^{[n^2-2n-1]},\ (n-2)^{[1]},\ n^{[2n-1]}\Big\}, & \text{if } n \geq 4 \text{ is even,} \\ \Big\{0^{[n^2-2n-1]},\ (n-1)^{[2]},\ n^{[2n-2]}\Big\}, & \text{if } n \geq 3 \text{ is odd.} \end{cases} \tag{6}$$

Proof. Write $L_n = L_{\mathrm{rc}} + D$, where $L_{\mathrm{rc}} = \sum_{i=1}^n \mathbf{r}_i\mathbf{r}_i^\top + \sum_{j=1}^n \mathbf{c}_j\mathbf{c}_j^\top$ and $D = \mathbf{d}_+\mathbf{d}_+^\top + \mathbf{d}_-\mathbf{d}_-^\top$. As the Cartesian product of two complete graphs $K_n \square K_n$, the operator L_{rc} has eigenvalues $2n$ (multiplicity 1, spanned by $\mathbf{1}$), n (multiplicity $2n-2$, spanned by zero-mean pure row functions $\mathcal{V}_{\mathrm{row}} = \{\mathbf{u} \otimes \mathbf{1}_n : \mathbf{u}^\top\mathbf{1}_n = 0\}$ and pure column functions $\mathcal{V}_{\mathrm{col}} = \{\mathbf{1}_n \otimes \mathbf{v} : \mathbf{v}^\top\mathbf{1}_n = 0\}$), and 0 (multiplicity $(n-1)^2$, the tensor-product subspace $\mathcal{V}_{\mathrm{row}} \otimes \mathcal{V}_{\mathrm{col}}$).

Because every row and every column intersects $\mathbf{d}_+$ and $\mathbf{d}_-$ in exactly one cell, $\mathbf{r}_i^\top\mathbf{d}_\pm = \mathbf{c}_j^\top\mathbf{d}_\pm = 1$ for all i, j. Thus for any zero-mean row or column mode $\mathbf{w} \in \mathcal{V}_{\mathrm{row}} \oplus \mathcal{V}_{\mathrm{col}} \subset \mathbf{1}^\perp$, we have $\mathbf{d}_+^\top\mathbf{w} = \mathbf{d}_-^\top\mathbf{w} = 0$. Consequently, the $(2n-2)$-dimensional subspace $\mathcal{V}_{\mathrm{row}} \oplus \mathcal{V}_{\mathrm{col}}$ is in the kernel of D and remains an exact eigenspace of both L_n and $\widetilde{L}_n$ with eigenvalue n and multiplicity $2n-2$.

It remains to analyze the action of L_n on the 3-dimensional subspace $\mathcal{S}_3 = \operatorname{span}\{\mathbf{1}, \mathbf{d}_+, \mathbf{d}_-\}$, which is orthogonal to $\mathcal{V}_{\mathrm{row}} \oplus \mathcal{V}_{\mathrm{col}}$. Introduce the symmetric and antisymmetric diagonal combinations $\mathbf{s}_d = \mathbf{d}_+ + \mathbf{d}_-$ and $\mathbf{a}_d = \mathbf{d}_+ - \mathbf{d}_-$. By symmetry, $\mathbf{1}^\top\mathbf{a}_d = 0$ and $L_{\mathrm{rc}}\mathbf{a}_d = 0$, so $\mathbf{a}_d \in \mathbf{1}^\perp$ is an exact eigenvector of both L_n and $\widetilde{L}_n$:

- For even n, $\mathbf{d}_+^\top\mathbf{d}_- = 0$, so $D\mathbf{a}_d = n\mathbf{a}_d$, contributing $+1$ to the multiplicity of eigenvalue n (giving $2n-1$ in total). For the symmetric mode $\mathbf{s}_d$, since $\mathbf{1}$ and $\mathbf{s}_d$ are linearly independent and every row and column intersects $\mathbf{s}_d$ in 2 cells, we have $L_{\mathrm{rc}}\mathbf{s}_d = 4\mathbf{1}$, $L_{\mathrm{rc}}\mathbf{1} = 2n\mathbf{1}$, $D\mathbf{1} = n\mathbf{s}_d$, and $D\mathbf{s}_d = n\mathbf{s}_d$. In the ordered basis $\mathcal{B} = (\mathbf{1}, \mathbf{s}_d)$, the coordinate matrix of L_n on $\operatorname{span}\{\mathbf{1}, \mathbf{s}_d\}$ is $[L_n]_{\mathcal{B}} = \left[\begin{smallmatrix} 2n & 4 \\ n & n \end{smallmatrix}\right]$, whose characteristic polynomial is $\lambda^2 - 3n\lambda + 2n(n-2) = 0$, yielding $\lambda_\pm(n) = \frac{3n \pm \sqrt{n(n+16)}}{2}$. Projecting onto $\mathbf{1}^\perp$ replaces $\mathbf{s}_d$ by $\widetilde{\mathbf{s}}_d = P_{\mathbf{1}^\perp}\mathbf{s}_d = \mathbf{s}_d - \frac{2}{n}\mathbf{1}$. Since $\mathbf{r}_i^\top\widetilde{\mathbf{s}}_d = \mathbf{c}_j^\top\widetilde{\mathbf{s}}_d = 2 - \frac{2}{n}(n) = 0$ for all i, j, we have $\widetilde{\mathbf{s}}_d \in \mathcal{V}_{\mathrm{row}} \otimes \mathcal{V}_{\mathrm{col}} = \ker(L_{\mathrm{rc}})$, so $L_{\mathrm{rc}}\widetilde{\mathbf{s}}_d = 0$. Moreover, $D\widetilde{\mathbf{s}}_d = D\mathbf{s}_d - \frac{2}{n}D\mathbf{1} = n\mathbf{s}_d - 2\mathbf{s}_d = (n-2)\mathbf{s}_d$, so $P_{\mathbf{1}^\perp}D\widetilde{\mathbf{s}}_d = (n-2)\widetilde{\mathbf{s}}_d$, yielding the exact integer eigenvalue $\mu = n-2$ with multiplicity 1.

- For odd n, $\mathbf{d}_+^\top\mathbf{d}_- = 1$ (shared central cell), so $\|\mathbf{a}_d\|^2 = 2(n-1)$ and $D\mathbf{a}_d = (n-1)\mathbf{a}_d$, giving eigenvalue $n-1$ for both L_n and $\widetilde{L}_n$. For the symmetric mode $\mathbf{s}_d$, $\mathbf{s}_d^\top\mathbf{s}_d = 2n+2$, so $D\mathbf{s}_d = (n+1)\mathbf{s}_d$ and the coordinate matrix of L_n in the basis $\mathcal{B} = (\mathbf{1}, \mathbf{s}_d)$ is $[L_n]_{\mathcal{B}} = \left[\begin{smallmatrix} 2n & 4 \\ n & n+1 \end{smallmatrix}\right]$ with characteristic polynomial $\lambda^2 - (3n+1)\lambda + 2n(n-1) = 0$, giving $\lambda_\pm(n) = \frac{3n+1 \pm \sqrt{n^2+14n+1}}{2}$. Projecting onto $\mathbf{1}^\perp$ gives $\widetilde{\mathbf{s}}_d = \mathbf{s}_d - \frac{2}{n}\mathbf{1} \in \ker(L_{\mathrm{rc}})$, on which $D\widetilde{\mathbf{s}}_d = (n+1)\mathbf{s}_d - 2\mathbf{s}_d = (n-1)\mathbf{s}_d$ and thus $\widetilde{L}_n\widetilde{\mathbf{s}}_d = (n-1)\widetilde{\mathbf{s}}_d$, contributing a second integer eigenvalue $\mu = n-1$ (total multiplicity 2).

Finally, the orthogonal complement of $\operatorname{span}\{\widetilde{\mathbf{s}}_d, \mathbf{a}_d\}$ inside the $(n-1)^2$-dimensional subspace $\mathcal{V}_{\mathrm{row}} \otimes \mathcal{V}_{\mathrm{col}}$ has dimension $(n-1)^2 - 2 = n^2 - 2n - 1$ and is annihilated by both L_{rc} and D, establishing Equation 4, Equation 5, and Equation 6. □

2.2 Universal Mean Eigenvalue and Random Permutation Ensemble Law

Theorem 2.1 reveals a remarkable parity-independent conservation law across all orders $n \geq 3$ (Table 2 and Figure 1a):

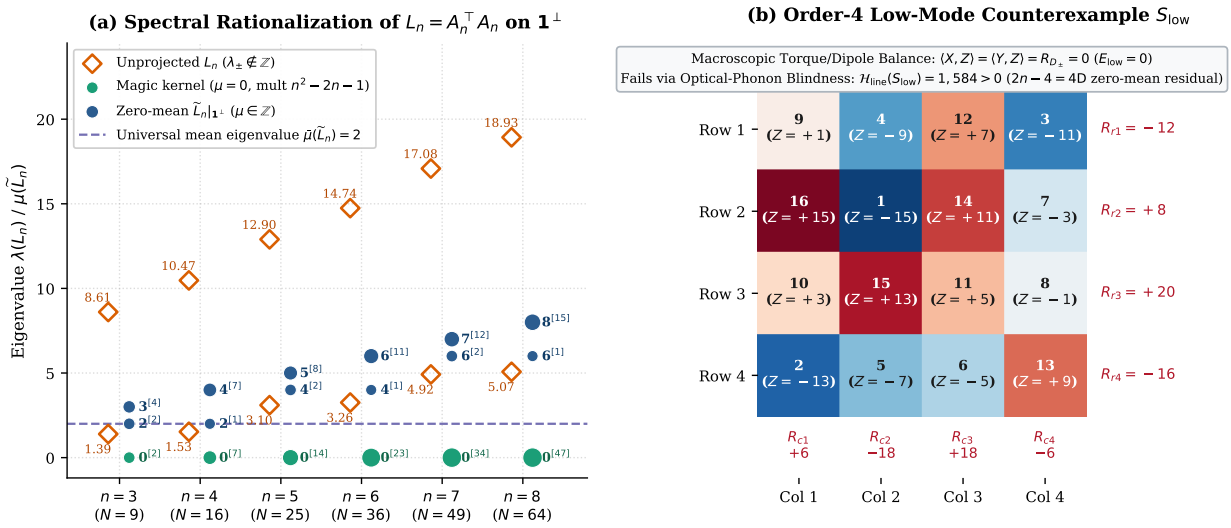


Figure 1: **Spectral rationalization of the line-incidence Laplacian $L_n = A_n^\top A_n$ and low-mode insufficiency.** **(a)** Comparison of the unprojected eigenvalues $\lambda(L_n)$ on $\mathbb{R}^{n^2}$ (hollow orange diamonds, showing the irrational branches $\lambda_\pm(n)$) against the zero-mean restricted spectrum $\mu(\widetilde{L}_n|_{\mathbf{1}^\perp})$ (filled navy and green circles, labeled $\mu^{[\text{mult}]}$) for orders $n = 3 \ldots 8$. Restricting to $\mathbf{1}^\perp$ collapses all eigenvalues into exact integers with universal mean $\bar{\mu}(\widetilde{L}_n) = 2$ (dashed purple line). **(b)** Explicit 4×4 low-mode counterexample S_{low} (Proposition 2.3) whose dipole moments $\langle X, Z\rangle = \langle Y, Z\rangle = 0$ and main diagonals $R_{D_\pm} = 0$ vanish ($E_{\text{low}} = 0$), yet whose high-frequency row and column residuals produce $\mathcal{H}_{\text{line}}(S_{\text{low}}) = 1{,}584 > 0$.

Theorem 2.2 (Universal Mean Eigenvalue and Ensemble Expectation)**.** *For every integer $n \geq 3$ (both odd and even), the trace of the zero-mean restricted Laplacian $\widetilde{L}_n$ on the (n^2-1)-dimensional hyperplane $\mathbf{1}^\perp$ is*

$$\operatorname{tr}\big(\widetilde{L}_n\big|_{\mathbf{1}^\perp}\big) = 2(n^2 - 1), \tag{7}$$

*so the mean eigenvalue of $\widetilde{L}_n$ on $\mathbf{1}^\perp$ is **identically** 2:*

$$\bar{\mu}(\widetilde{L}_n) = \frac{\operatorname{tr}(\widetilde{L}_n|_{\mathbf{1}^\perp})}{n^2 - 1} = 2. \tag{8}$$

Consequently, for a uniform random permutation $S \sim \text{Unif}(S_{n^2})$ with centred height vector $\mathbf{z}(S)$ of constant squared norm $\|\mathbf{z}\|^2 = \frac{1}{3}n^2(n^4 - 1)$, the expected line-indicator Hamiltonian is exactly twice the height variance sum:

$$\mathbb{E}_{S \sim \text{Unif}(S_{n^2})}\big[\mathcal{H}_{\text{line}}(S)\big] = \bar{\mu}(\widetilde{L}_n)\,\|\mathbf{z}\|^2 = 2\,\|\mathbf{z}\|^2 = \frac{2}{3}n^2(n^4 - 1). \tag{9}$$

Proof. We give both a direct parity-free trace proof and a spectral verification. On $\mathbb{R}^{n^2}$, each of the $2n + 2$ magic lines in $\mathcal{L}_n$ contains n unit entries, so $\operatorname{tr}(L_n) = \sum_{L \in \mathcal{L}_n} \|\mathbf{1}_L\|_2^2 = (2n + 2)n = 2n^2 + 2n$. Meanwhile, the normalized constant vector $\hat{\mathbf{1}} = \frac{1}{n}\mathbf{1}$ has Rayleigh quotient $\hat{\mathbf{1}}^\top L_n \hat{\mathbf{1}} = \frac{1}{n^2}\sum_{L \in \mathcal{L}_n}(\mathbf{1}_L^\top \mathbf{1})^2 = \frac{1}{n^2}(2n + 2)n^2 = 2n + 2$. Subtracting the constant mode on $\mathbf{1}^\perp$ immediately yields, for all $n \geq 3$ regardless of parity,

$$\operatorname{tr}\big(\widetilde{L}_n\big|_{\mathbf{1}^\perp}\big) = \operatorname{tr}(L_n) - \hat{\mathbf{1}}^\top L_n \hat{\mathbf{1}} = (2n^2 + 2n) - (2n + 2) = 2(n^2 - 1),$$

which agrees with summing the integer eigenvalues in Theorem 2.1: $(n-2) + (2n-1)n = 2(n^2-1)$ for even n and $2(n - 1) + (2n - 2)n = 2(n^2 - 1)$ for odd n. Dividing by $\dim(\mathbf{1}^\perp) = n^2 - 1$ gives $\bar{\mu}(\widetilde{L}_n) = 2$. Under the uniform distribution on S_{n^2}, the covariance matrix of $\mathbf{z}(S)$ is isotropic on $\mathbf{1}^\perp$: $\mathbb{E}[\mathbf{z}\mathbf{z}^\top] = \frac{\|\mathbf{z}\|^2}{n^2-1} P_{\mathbf{1}^\perp}$ [7]. Therefore $\mathbb{E}[\mathbf{z}^\top L_n \mathbf{z}] = \operatorname{tr}(L_n \mathbb{E}[\mathbf{z}\mathbf{z}^\top]) = \frac{\|\mathbf{z}\|^2}{n^2-1}\operatorname{tr}(\widetilde{L}_n|_{\mathbf{1}^\perp}) = 2\|\mathbf{z}\|^2 = \frac{2}{3}n^2(n^4 - 1)$. □

Table 2: Exact spectral invariants of the unprojected Laplacian L_n on $\mathbb{R}^{n^2}$ and rationalized zero-mean Laplacian $\widetilde{L}_n$ on $\mathbf{1}^\perp$ across orders $n = 3 \dots 8$, verified by `verify_paper_d.py`.

n	$N = n^2$	$\operatorname{rank}(A_n)$	$\dim\ker(L_n)$	Irrational $\lambda_\pm(L_n)$	Zero-Mean $\operatorname{spec}(\widetilde{L}_n\|_{\mathbf{1}^\perp})$	$\operatorname{tr}(\widetilde{L}_n)$	$\mathbb{E}[\mathcal{H}_{\text{line}}(S)] = 2\|\mathbf{z}\|^2$
3	9	7	2	1.3944, 8.6056	$\{0^{[2]}, 2^{[2]}, 3^{[4]}\}$	16	480
4	16	9	7	1.5279, 10.4721	$\{0^{[7]}, 2^{[1]}, 4^{[7]}\}$	30	2,720
5	25	11	14	3.1010, 12.8990	$\{0^{[14]}, 4^{[2]}, 5^{[8]}\}$	48	10,400
6	36	13	23	3.2554, 14.7446	$\{0^{[23]}, 4^{[1]}, 6^{[11]}\}$	70	31,080
7	49	15	34	4.9172, 17.0828	$\{0^{[34]}, 6^{[2]}, 7^{[12]}\}$	96	78,400
8	64	17	47	5.0718, 18.9282	$\{0^{[47]}, 6^{[1]}, 8^{[15]}\}$	126	174,720

2.3 Low-Mode Insufficiency and the $(2n-4)$-Dimensional Zero-Mean Optical-Phonon Subspace

In Paper II [14] and Paper III [13], we proved that semi-magic row and column balance implies vanishing dipole covariance $\langle X, Z\rangle = \langle Y, Z\rangle = 0$, so that every magic square has an isotropic inertia tensor. A natural physical question is whether the converse holds when supplemented by the two main diagonal constraints: if a permutation $S \in S_{n^2}$ satisfies zero dipole tilt ($\langle X, Z\rangle = \langle Y, Z\rangle = 0$) and zero diagonal residuals ($R_{D_+} = R_{D_-} = 0$), must S be a magic square? By Theorem 2.1, the answer is emphatically negative for all $n \geq 3$:

Proposition 2.3 (Low-Mode Insufficiency and Explicit Order-4 Counterexample)**.** *Define the* 4*-mode dipole-plus-diagonal energy functional*

$$E_{\text{low}}(S) = \langle X, Z\rangle^2 + \langle Y, Z\rangle^2 + R_{D_+}(S)^2 + R_{D_-}(S)^2. \tag{10}$$

For any order $n \geq 3$, the four zero-mean vectors $\{X, Y, \widetilde{\mathbf{d}}_+, \widetilde{\mathbf{d}}_-\}$ (where $\widetilde{\mathbf{d}}_\pm = P_{\mathbf{1}^\perp}\mathbf{d}_\pm = \mathbf{d}_\pm - \frac{1}{n}\mathbf{1}$) are linearly independent and span a 4*-dimensional subspace of the $2n$-dimensional active zero-mean image $\operatorname{im}(\widetilde{L}_n) \subset \mathbf{1}^\perp$ (and a* 4*-dimensional subspace of the $(2n+1)$-dimensional unprojected image $\operatorname{im}(L_n) \subset \mathbb{R}^{n^2}$). Consequently, its orthogonal complement within $\operatorname{im}(\widetilde{L}_n) \subset \mathbf{1}^\perp$ has dimension*

$$\dim\big(\operatorname{im}(\widetilde{L}_n) \cap \ker(E_{\text{low}})\big) = 2n-4 = 2(n-2) \quad \big(\text{or } (2n+1)-4 = 2n-3 \text{ in } \operatorname{im}(L_n) \subset \mathbb{R}^{n^2}\big), \tag{11}$$

spanned by the $n-2$ higher-degree orthogonalized column polynomial modes $P_k(X) \in \mathcal{V}_{\text{col}}$ and $n-2$ row polynomial modes $P_k(Y) \in \mathcal{V}_{\text{row}}$ for $2 \leq k \leq n-1$. At order $n = 4$ ($2n-4 = 4$ zero-mean optical modes), the explicit permutation

$$S_{\text{low}} = \begin{bmatrix} 9 & 4 & 12 & 3 \\ 16 & 1 & 14 & 7 \\ 10 & 15 & 11 & 8 \\ 2 & 5 & 6 & 13 \end{bmatrix} \in S_{16} \tag{12}$$

satisfies $\langle X, Z\rangle = 0$, $\langle Y, Z\rangle = 0$, $R_{D_+}(S_{\text{low}}) = 0$, and $R_{D_-}(S_{\text{low}}) = 0$ ($E_{\text{low}}(S_{\text{low}}) = 0$), yet exhibits non-zero row residuals $\mathbf{R}_{\text{row}} = (-12, +8, +20, -16)$, column residuals $\mathbf{R}_{\text{col}} = (+6, -18, +18, -6)$, and total line energy $\mathcal{H}_{\text{line}}(S_{\text{low}}) = 1{,}584 > 0$ (Figure 1b).

Proof. Because $X \in \mathcal{V}_{\text{col}}$ and $Y \in \mathcal{V}_{\text{row}}$ are non-zero pure column and pure row vectors, they are orthogonal to each other and to $\widetilde{\mathbf{d}}_+, \widetilde{\mathbf{d}}_- \in \mathcal{V}_{\text{row}} \otimes \mathcal{V}_{\text{col}}$. Since $\widetilde{\mathbf{d}}_+$ and $\widetilde{\mathbf{d}}_-$ are linearly independent for all $n \geq 3$, $\{X, Y, \widetilde{\mathbf{d}}_+, \widetilde{\mathbf{d}}_-\}$ spans a 4-dimensional subspace of $\operatorname{im}(\widetilde{L}_n) = \mathcal{V}_{\text{row}} \oplus \mathcal{V}_{\text{col}} \oplus \operatorname{span}\{\widetilde{\mathbf{s}}_d, \mathbf{a}_d\}$. Because $\dim\operatorname{im}(\widetilde{L}_n) = \operatorname{rank}(\widetilde{L}_n) = 2n$ on $\mathbf{1}^\perp$ by Theorem 2.1 (while $\operatorname{rank}(L_n) = 2n+1$ on $\mathbb{R}^{n^2}$ when including the constant vector $\mathbf{1}$), the zero-mean high-frequency residual subspace inside $\operatorname{im}(\widetilde{L}_n)$ has dimension $2n-4 = 2(n-2)$, consisting of the $(n-2)$-dimensional complement of $\operatorname{span}\{Y\}$ in $\mathcal{V}_{\text{row}}$ plus the $(n-2)$-dimensional complement of $\operatorname{span}\{X\}$ in $\mathcal{V}_{\text{col}}$. Direct evaluation on S_{low} in Equation 12 yields row sums $(28, 38, 44, 26)$ (centred residuals $(-12, 8, 20, -16)$), column sums $(37, 25, 43, 31)$ (centred residuals $(6, -18, 18, -6)$), and diagonal sums $(34, 34)$ (centred residuals $(0, 0)$). Taking inner products with $X = (-3, -1, 1, 3)$ and $Y = (3, 1, -1, -3)$ gives $\langle X, Z\rangle = -3(6) - 1(-18) + 1(18) + 3(-6) = 0$ and $\langle Y, Z\rangle = 3(-12) + 1(8) - 1(20) - 3(-16) = 0$, while $\mathcal{H}_{\text{line}}(S_{\text{low}}) = (-12)^2 + 8^2 + 20^2 + (-16)^2 + 6^2 + (-18)^2 + 18^2 + (-6)^2 = 1{,}584$. □

From a physical standpoint, Proposition 2.3 explains why *macroscopic rigid-body torque and moment-of-inertia solvers fail* to synthesize magic squares: a physical solver that couples only to global center-of-mass tilt ($\langle X, Z\rangle, \langle Y, Z\rangle$) and principal diagonal moments ($R_{D_\pm}$) constrains only the 4 long-wavelength "acoustic" modes in $\mathbf{1}^\perp$ and is completely blind to the $2n-4$ short-wavelength zero-mean "optical phonon" modes ($\langle X^k, Z\rangle, \langle Y^k, Z\rangle$ for $2 \le k \le n-1$). Conversely, Theorem 2.1 also governs the *Maxwell–Calladine constraint-counting ratio* [17, 4] on the zero-mean hyperplane $\mathbf{1}^\perp$:

$$\eta_{\mathrm{MC}}(n) = \frac{\dim\ker(\widetilde{L}_n)}{\mathrm{rank}(\widetilde{L}_n)} = \frac{n^2 - 2n - 1}{2n}, \tag{13}$$

which measures the ratio of internal zero-energy "floppy modes" ($\dim\ker(\widetilde{L}_n)$) to active zero-mean linear constraints ($\mathrm{rank}(\widetilde{L}_n) = \mathrm{rank}(A_n) - 1 = 2n$). For $n = 3$ ($\eta_{\mathrm{MC}} = 2/6 = 0.33$) and $n = 4$ ($\eta_{\mathrm{MC}} = 7/8 = 0.88$), the system is *overconstrained* ($\eta_{\mathrm{MC}} < 1$). The isostatic crossover $\eta_{\mathrm{MC}} \approx 1$ occurs between $n = 4$ and $n = 5$ ($\eta_{\mathrm{MC}}(5) = 14/10 = 1.40$), where discrete permutation frustration reaches its maximum, before entering an *underconstrained floppy regime* at $n \ge 6$ ($\eta_{\mathrm{MC}}(6) = 1.92$, $\eta_{\mathrm{MC}}(7) = 2.43$, $\eta_{\mathrm{MC}}(8) = 2.94$) that drives the Dimensional Relief Phenomenon in Section 5.

3 Multiscale Window Entropies and 2×2 Quartet Equivalence

Once a permutation reaches the magic ground-state manifold $\ker(\widetilde{L}_n)$ where $\mathcal{H}_{\mathrm{line}}(S) = 0$, all $2n+2$ global 1D line sums are identical. However, distinct magic squares of the same order exhibit vastly different local 2D spatial organization [8, 19, 5]. To resolve this internal structure across scales, we introduce sliding $k \times k$ sub-window energies and Shannon entropies, and evaluate them exhaustively across all 880 Frénicle order-4 magic squares and higher-order constructive families.

3.1 Sliding-Window Shannon Entropy and Constructive Family Scaling

For any scale $k \in \{1, \dots, n\}$, an $n \times n$ grid contains $M_k = (n-k+1)^2$ interior contiguous $k \times k$ sub-windows $W_{r,c}^{(k)} = \{r, \dots, r+k-1\} \times \{c, \dots, c+k-1\}$ ($1 \le r, c \le n-k+1$). For any exponent $p \in \{1, 2, 4\}$, define the local ℓ_p^p window weight and normalized Shannon window entropy by

$$w_p\big(W_{r,c}^{(k)}\big) = \sum_{(i,j)\in W_{r,c}^{(k)}} |Z_{ij}|^p, \qquad p_{r,c}^{(k)} = \frac{w_p(W_{r,c}^{(k)})}{\sum_{r',c'} w_p(W_{r',c'}^{(k)})}, \qquad \widetilde{H}_p(k) = \frac{-\sum_{r,c} p_{r,c}^{(k)} \log_2 p_{r,c}^{(k)}}{\log_2\big((n-k+1)^2\big)}. \tag{14}$$

Here $\widetilde{H}_p(k) \in (0, 1]$ measures the spatial uniformity of height magnitude across all $k \times k$ sub-windows ($\widetilde{H}_p(k) = 1$ if and only if every $k \times k$ window carries identical ℓ_p^p weight).

Figure 2a and Table 3 compare the multiscale entropy profile $\widetilde{H}_p(k)$ across five classical constructive families: odd-order de La Loubère (Siamese) squares ($n = 3, 5$) [6], doubly-even 4×4 diagonal-mask squares ($n = 4, 8$) [1], and Conway's LUX singly-even construction ($n = 6$) [2]. At $k = 2$, the 3×3 Lo Shu square achieves the highest local uniformity ($\widetilde{H}_1(2) = 0.99435$, $\widetilde{H}_2(2) = 0.99073$), whereas doubly-even mask constructions at $n = 4, 8$ concentrate extreme values symmetrically in corner and central blocks, lowering $\widetilde{H}_2(2)$ to 0.91498 ($n = 4$) and 0.90598 ($n = 8$). Crucially, while $n = 3, 4, 5, 8$ constructions are centrosymmetric ($B_{\mathrm{comp}} = 0$ complement breaks and $M_{xyz} = 0$), Conway's $n = 6$ LUX method breaks all 18/18 antipodal complement pairs and generates a non-zero mixed octupole moment $M_{xyz} = -132$.

3.2 Equivalence of Interior and Toroidal 2×2 Quartet Balance at Order 4

Beyond magnitude entropy, the signed sum of each 2×2 quartet $Q_{r,c}(S) = Z_{r,c} + Z_{r+1,c} + Z_{r,c+1} + Z_{r+1,c+1}$ (with indices taken modulo n in the toroidal case) defines the *interior* and *toroidal* 2×2

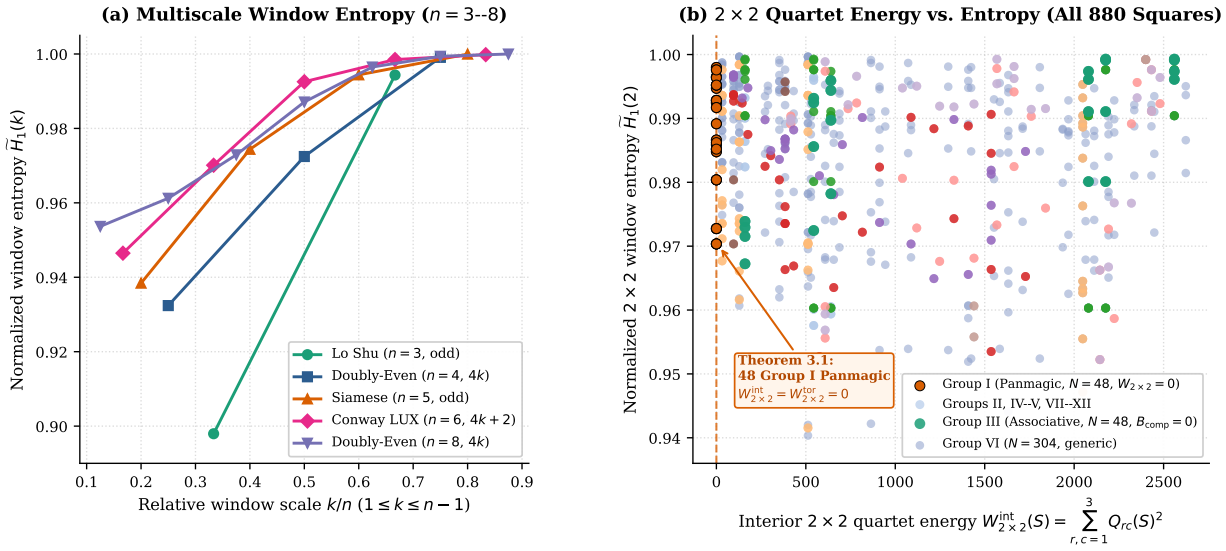


Figure 2: **Multiscale sliding-window Shannon entropy and 2×2 quartet energy census. (a)** Normalized ℓ_1 window entropy $\widetilde{H}_1(k)$ versus relative scale k/n across five constructive magic-square families ($n = 3$ Lo Shu, $n = 4, 8$ Doubly-Even, $n = 5$ Siamese, and $n = 6$ Conway LUX). **(b)** Joint distribution of interior 2×2 quartet residual energy $W^{\text{int}}_{2\times 2}(S)$ and window entropy $\widetilde{H}_1(2)$ across all 880 Frénicle order-4 magic squares partitioned by Dudeney Groups I–XII, illustrating Theorem 3.1: $W^{\text{int}}_{2\times 2}(S) = 0$ holds if and only if $W^{\text{tor}}_{2\times 2}(S) = 0$, isolating the 48 panmagic squares of Group I.

Table 3: Multiscale window entropy $\widetilde{H}_p(2)$, interior and toroidal 2×2 quartet energies $W_{2\times 2}$, complement breaks B_{comp}, and mixed octupole moment M_{xyz} across constructive magic square families ($n = 3 \ldots 8$).

Family	Order / Class	$\widetilde{H}_1(2)$	$\widetilde{H}_2(2)$	$W^{\text{int}}_{2\times 2}(S)$	$W^{\text{tor}}_{2\times 2}(S)$	Breaks B_{comp}	Octupole M_{xyz}
Lo Shu (Siamese)	$n = 3$ (odd)	0.99435	0.99073	80	240	0/4	0
Doubly-Even Mask	$n = 4$ $(4k)$	0.97245	0.91498	544	1,088	0/8	0
Siamese (de La Loubère)	$n = 5$ (odd)	0.97438	0.94254	16,320	25,200	0/12	0
Conway LUX Method	$n = 6$ $(4k + 2)$	0.97011	0.93161	84,640	97,440	18/18	−132
Doubly-Even Mask	$n = 8$ $(4k)$	0.96123	0.90598	112,320	149,760	0/32	0

quartet energies:

$$W^{\text{int}}_{2\times 2}(S) = \sum_{r=1}^{n-1}\sum_{c=1}^{n-1} Q_{r,c}(S)^2, \qquad W^{\text{tor}}_{2\times 2}(S) = \sum_{r=1}^{n}\sum_{c=1}^{n} Q_{r,c}(S)^2. \tag{15}$$

At order $n = 4$, $W^{\text{int}}_{2\times 2}$ sums over the 9 interior 2×2 blocks, whereas $W^{\text{tor}}_{2\times 2}$ includes the 7 boundary-wrapping blocks. We prove that on the order-4 magic manifold, interior quartet balance automatically implies full toroidal quartet balance:

Theorem 3.1 (Interior–Toroidal 2×2 Quartet Equivalence)**.** *Let S be any magic square of even order $n = 2m \ge 4$. Then its $(2m-1)^2$ interior 2×2 blocks have zero centred sum ($W^{\text{int}}_{2\times 2}(S) = 0$) **if and only if** all $4m^2$ toroidal 2×2 blocks have zero centred sum ($W^{\text{tor}}_{2\times 2}(S) = 0$). In particular, across the 880 Frénicle magic squares of order $n = 4$, vanishing of the 9 interior quartets ($W^{\text{int}}_{2\times 2}(S) = 0$) is equivalent to vanishing of all 16 toroidal quartets ($W^{\text{tor}}_{2\times 2}(S) = 0$) and holds on **exactly the** 48 **panmagic (diabolic) squares of Dudeney Group I** (Figure 2b and Table 4).*

Proof. Clearly $W^{\text{tor}}_{2\times 2}(S) = 0 \implies W^{\text{int}}_{2\times 2}(S) = 0$. Conversely, suppose S is a magic square of even order $n = 2m$ ($\mathcal{H}_{\text{line}}(S) = 0$) with $Q_{r,c}(S) = 0$ for all interior blocks $1 \le r, c \le 2m-1$. For any horizontally wrapping 2×2 block $Q_{r,2m}(S)$ $(1 \le r \le 2m-1)$, the sum of rows r and $r+1$ vanishes

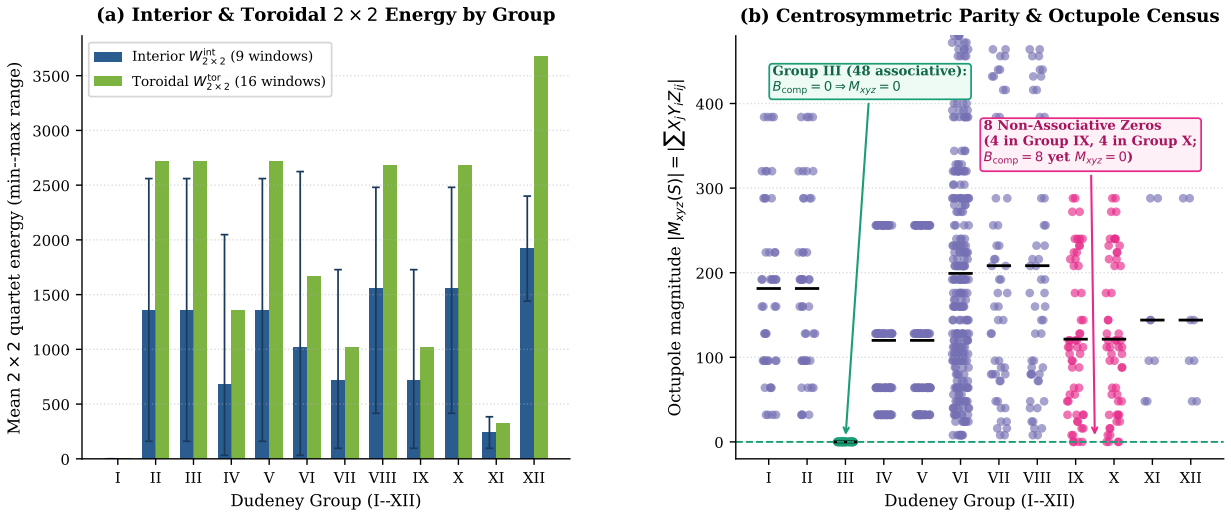


Figure 3: **Group-resolved 2×2 quartet energies and mixed octupole census across Dudeney Groups I–XII. (a)** Mean interior $W^{\text{int}}_{2\times2}$ (9 windows, navy bars with min–max range) and toroidal $W^{\text{tor}}_{2\times2}$ (16 windows, green bars) across the 12 Dudeney groups. **(b)** Magnitude of the mixed octupole moment $|M_{xyz}(S)| = |\sum X_j Y_i Z_{ij}|$ across all 880 squares (Proposition 3.2), highlighting the 48 associative squares of Group III ($B_{\text{comp}} = 0 \implies M_{xyz} = 0$) and the 8 anomalous non-associative octupole-zero squares in Groups IX and X ($B_{\text{comp}} = 8$ yet $M_{xyz} = 0$ via the Concentric Shell Quadrupole resonance $8Q_{\text{corner}} = -3Q_{\text{edge}}$).

by magic row balance and partitions into m disjoint 2×2 blocks starting at even columns:

$$0 = R_{r_r}(S) + R_{r_{r+1}}(S) = \sum_{j=1}^{m-1} Q_{r,2j-1}(S) + Q_{r,2m-1}(S) = \sum_{j=1}^{m-1} Q_{r,2j}(S) + Q_{r,2m}(S). \tag{16}$$

Since $Q_{r,2j}(S) = 0$ for all $1 \le j \le m-1$ by interior balance, Equation 16 forces $Q_{r,2m}(S) = 0$ for all $1 \le r \le 2m-1$. Symmetrically, summing columns c and $c+1$ gives $0 = R_{c_c}(S) + R_{c_{c+1}}(S) = \sum_{i=1}^{m-1} Q_{2i,c}(S) + Q_{2m,c}(S)$, so $Q_{2m,c}(S) = 0$ for all $1 \le c \le 2m-1$. Finally, the corner-wrapping quartet $Q_{2m,2m}(S)$ satisfies $Q_{2m,2m}(S) = (R_{r_1}(S) + R_{r_{2m}}(S)) - \sum_{j=1}^{m-1} Q_{2m,2j}(S) = 0 - 0 = 0$. Thus all $4m^2$ toroidal quartets vanish. At $n = 4$ ($m = 2$), it is a classical theorem of Frénicle and Dudeney [8, 19] that $W^{\text{tor}}_{2\times2}(S) = 0$ holds if and only if S is panmagic, isolating the 48 squares of Dudeney Group I. □

3.3 Complement Parity and the Concentric Shell Quadrupole Identity

In Paper II [14] and Paper III [13], the mixed third-order moment (octupole) $M_{xyz}(S) = \sum_{i,j=1}^{n} X_j Y_i Z_{ij}$ governed the asymmetry between static and dynamic axes. To connect $M_{xyz}(S)$ to discrete cell pairing, define the *complement-break count* $B_{\text{comp}}(S)$ as the number of antipodal cell pairs $\{(i,j), (n+1-i, n+1-j)\}$ that fail the associative condition $Z_{ij} + Z_{n+1-i,n+1-j} = 0$ ($s_{ij} + s_{n+1-i,n+1-j} = n^2 + 1$). We now prove an exact Diophantine decomposition that explains both the symmetry-protected and accidental octupole zeros at order 4:

Proposition 3.2 (Concentric Shell Quadrupole Identity and Octupole Zero Classification)**.** *For any order-4 magic square S, partition the 16 cells into the 4 outer corners ($|X_j Y_i| = 9$), the 8 non-corner boundary edge cells ($|X_j Y_i| = 3$), and the 4 inner 2×2 cells ($|X_j Y_i| = 1$), with signed quadrupolar moments*

$$Q_{\text{corner}}(S) = (Z_{11} + Z_{44}) - (Z_{14} + Z_{41}), \qquad Q_{\text{inner}}(S) = (Z_{22} + Z_{33}) - (Z_{23} + Z_{32}),$$
$$Q_{\text{edge}}(S) = \big[(Z_{12} + Z_{43}) - (Z_{13} + Z_{42})\big] + \big[(Z_{21} + Z_{34}) - (Z_{31} + Z_{24})\big]. \tag{17}$$

Then across all 880 Frénicle magic squares of order 4:

Table 4: Complete multiscale window and multipole census across the 12 Dudeney groups of the 880 order-4 magic squares, verified by `verify_paper_d.py`.

Dudeney Group	N_g	B_{comp}	Mean $\widetilde{H}_1(2)$	Mean $\widetilde{H}_2(2)$	$W^{\text{int}}_{2\times2}$ (mean [min, max])	$W^{\text{tor}}_{2\times2}$ (mean)	$\lvert M_{xyz}\rvert$ (mean, $\#=0$)
I (Panmagic)	48	8	0.98722	0.96742	0.0 [0, 0]	0.0	181.3 (0/48)
II (Semi-pan.)	48	8	0.98148	0.95260	1360.0 [160, 2560]	2720.0	181.3 (0/48)
III (Assoc.)	48	0	0.98807	0.96789	1360.0 [160, 2560]	2720.0	0.0 (48/48)
IV	96	8	0.97919	0.94745	680.0 [32, 2048]	1360.0	120.0 (0/96)
V	96	8	0.98831	0.96951	1360.0 [160, 2560]	2720.0	120.0 (0/96)
VI	304	8	0.98356	0.95870	1017.7 [32, 2624]	1671.2	199.2 (0/304)
VII	56	8	0.97874	0.94983	720.6 [96, 1728]	1015.4	208.3 (0/56)
VIII	56	8	0.98127	0.95081	1554.9 [416, 2480]	2684.0	208.3 (0/56)
IX	56	8	0.98432	0.95886	720.6 [96, 1728]	1015.4	121.4 (4/56)
X	56	8	0.98705	0.96844	1554.9 [416, 2480]	2684.0	121.4 (4/56)
XI	8	8	0.98516	0.96109	240.0 [96, 384]	320.0	144.0 (0/8)
XII	8	8	0.97871	0.94441	1920.0 [1440, 2400]	3680.0	144.0 (0/8)

1. ***Binary Complement Breaking:*** *The complement-break count* $B_{\text{comp}}(S) \in \{0, 1, \ldots, 8\}$ *takes* ***only the two extreme values*** $\{0, 8\}$*:* $B_{\text{comp}}(S) = 0$ *on the* 48 *associative squares of Dudeney Group III, and* $B_{\text{comp}}(S) = 8$ *on all remaining* 832 *squares (where the* 8 *complement pairs follow non-antipodal regular* 2*-factors of the* 4×4 *grid [8]).*

2. ***Concentric Shell Quadrupole Identity:*** *Diagonal balance* $R_{D_+}(S) = R_{D_-}(S) = 0$ *forces the exact identity* $Q_{\text{inner}}(S) = -Q_{\text{corner}}(S)$*, reducing the mixed octupole moment of every* 4×4 *magic square to the Diophantine linear form*

$$M_{xyz}(S) = -9\,Q_{\text{corner}}(S) - 3\,Q_{\text{edge}}(S) - Q_{\text{inner}}(S) = -8\,Q_{\text{corner}}(S) - 3\,Q_{\text{edge}}(S). \tag{18}$$

3. ***Complete Classification of Octupole Zeros (***56/880 ***Squares):*** *By Equation 18,* $M_{xyz}(S) = 0 \iff 8\,Q_{\text{corner}}(S) = -3\,Q_{\text{edge}}(S)$*, which holds on* ***exactly*** 56 ***of the*** 880 ***squares*** *(Figure 3b and Table 4):*

   - Symmetry-protected zeros (48 squares, Group III): *Associative parity* $Z_{5-i,5-j} = -Z_{ij}$ *forces* $Q_{\text{corner}}(S) = Q_{\text{edge}}(S) = 0$ *identically.*
   - Forbidden groups (288 squares, Groups I, II, IV, V): *Complement pairings along rows, columns, or* 2×2 *blocks force* $Q_{\text{edge}}(S) = 0$ *while* $Q_{\text{corner}}(S) \neq 0$*, so* $M_{xyz}(S) = -8\,Q_{\text{corner}}(S) \neq 0$ *can never vanish.*
   - Coprime shell-resonance zeros (8 non-associative squares, Groups IX and X): *Exactly* 4 *squares in Group IX (Frénicle* ***#200, #208, #390, #711****) and* 4 *squares in Group X (*`#492, #494, #794, #811`*) satisfy the coprime integer resonance* $\big(Q_{\text{corner}}(S), Q_{\text{edge}}(S)\big) = (-3k, 8k)$ *at* $k = \pm 4$ *(*`#208, #711, #492, #494`*) and* $k = -8$ *(*`#200, #390, #794, #811`*), mapped bijectively between Groups IX and X by the simultaneous row/column parity permutation* $\pi = (2, 4, 1, 3)$ *and paired within each group by complementation* $S \leftrightarrow 171 - S$*.*

Proof. Since $R_{D_+}(S) = (Z_{11} + Z_{44}) + (Z_{22} + Z_{33}) = 0$ and $R_{D_-}(S) = (Z_{14} + Z_{41}) + (Z_{23} + Z_{32}) = 0$, subtracting the two equations yields $Q_{\text{inner}}(S) = (Z_{22} + Z_{33}) - (Z_{23} + Z_{32}) = -(Z_{11} + Z_{44}) + (Z_{14} + Z_{41}) = -Q_{\text{corner}}(S)$. Expanding $M_{xyz}(S) = \sum_{i,j=1}^{4} X_j Y_i Z_{ij}$ with $(X_1, X_2, X_3, X_4) = (-3, -1, 1, 3)$ and $(Y_1, Y_2, Y_3, Y_4) = (3, 1, -1, -3)$ gives $M_{xyz}(S) = -9\,Q_{\text{corner}}(S) - 3\,Q_{\text{edge}}(S) - Q_{\text{inner}}(S) = -8\,Q_{\text{corner}}(S) - 3\,Q_{\text{edge}}(S)$. Because $\gcd(8, 3) = 1$, vanishing of $M_{xyz}(S)$ requires $Q_{\text{corner}}(S) = -3k$ and $Q_{\text{edge}}(S) = 8k$ for some integer $k \in \mathbb{Z}$, verified exhaustively across all 880 squares in `verify_paper_d.py`. □

Across all 880 squares, the global maximum of 2×2 window entropy is achieved by Frénicle square `#123` in Group VI ($\widetilde{H}_1(2) = 0.999669$), while the global minimum occurs at square `#599` in Group VI ($\widetilde{H}_1(2) = 0.940345$). Notice also in Table 4 and Figure 3a that Groups II, III, and V share the exact same mean interior quartet energy $\langle W^{\text{int}}_{2\times2} \rangle = 1{,}360 = \|\mathbf{z}\|^2$ and mean toroidal quartet energy $\langle W^{\text{tor}}_{2\times2} \rangle = 2{,}720 = 2\|\mathbf{z}\|^2$.

4 Combinatorial Swap Landscape and Antipodal Traps

Whereas Section 2 showed that the continuous quadratic form $\mathbf{z}^\top L_n \mathbf{z}$ on $\mathbf{1}^\perp$ is convex and barrier-free, restricting $\mathbf{z}$ to the discrete permutation polytope S_{n^2} induces a rugged combinatorial energy landscape under elementary cell swaps. We now derive the exact algebraic law governing 2-cycle transpositions and perform an exhaustive basin census of S_9 ($n = 3$) and a large-scale relaxation census of S_{16} ($n = 4$).

4.1 Exact Quadratic Transposition Law

Let $\mathbf{g}(S) = \frac{1}{2}\nabla\mathcal{H}_{\text{line}}(\mathbf{z}) = L_n\mathbf{z} = A_n^\top \mathbf{R}(S) \in \mathbb{Z}^{n^2}$ denote the *cell-stress vector*, whose component $g_a(S) = \sum_{L \ni a} R_L(S)$ at cell $a \in \{1, \dots, n^2\}$ is the sum of the centred residuals of the 2, 3, or 4 magic lines passing through cell a. Swapping the values at cells a and b via the transposition $\tau_{ab} \in S_{n^2}$ replaces $\mathbf{z}$ by $\mathbf{z}' = \mathbf{z} - d(\mathbf{e}_a - \mathbf{e}_b)$, where $d = Z_a - Z_b = 2(s_a - s_b)$. Expanding $\mathbf{z}'^\top L_n \mathbf{z}'$ yields:

Proposition 4.1 (Exact Transposition Energy Formula)**.** *For any permutation $S \in S_{n^2}$ and any pair of cells $a \neq b$ with height difference $d = Z_a - Z_b$, the change in the line-indicator Hamiltonian under the transposition τ_{ab} is*

$$\Delta\mathcal{H}_{\text{line}}(\tau_{ab}) = \mathcal{H}_{\text{line}}(\tau_{ab}S) - \mathcal{H}_{\text{line}}(S) = -2d\big(g_a(S) - g_b(S)\big) + c_{ab}\, d^2, \tag{19}$$

where $c_{ab} = (L_n)_{aa} + (L_n)_{bb} - 2(L_n)_{ab} = \|A_n(\mathbf{e}_a - \mathbf{e}_b)\|_2^2 \in \{2, 3, 4, 5, 6, 7\}$ counts the number of magic lines in $\mathcal{L}_n$ that pass through exactly one *of the two distinct cells a and b ($c_{ab} \in \{3, 4, 5, 6\}$ for $n = 3$, $\{2, 3, 4, 5, 6\}$ for even $n \geq 4$, and $\{2, 3, 4, 5, 6, 7\}$ for odd $n \geq 5$, since only the unique central cell of odd n lies on all 4 lines). In particular, $\Delta\mathcal{H}_{\text{line}}(\tau_{ab}) < 0$ if and only if $(g_a - g_b)/d > c_{ab}/2$.*

Proposition 4.1 is the exact combinatorial counterpart of *Kawasaki spin-exchange dynamics* in conserved-order-parameter lattice gases [11]: a particle exchange τ_{ab} is driven by the local chemical-potential / stress gradient $-2d(g_a - g_b)$ but opposed by the quadratic self-energy barrier $c_{ab}d^2$ of the c_{ab} magic lines severed by the jump. When line residuals $R_L(S)$ are small (± 2 in centred units, or ± 1 in standard units), the linear stress release $-2d(g_a - g_b)$ has magnitude $O(|d|)$, whereas the self-energy penalty $c_{ab}d^2 \geq 8$ (since $|d| \geq 2$ and $c_{ab} \geq 2$) grows quadratically with the height jump $|d|$ and freezes Kawasaki 2-cycle relaxation in kinetic traps.

4.2 Exhaustive S_9 Landscape Census and the 8 Antipodal Traps of Order 3

At order $n = 3$, the symmetric group S_9 has $9! = 362{,}880$ states, permitting an exact, exhaustive classification of the entire combinatorial energy landscape (Theorem 4.2 and Figure 4):

Theorem 4.2 (Exhaustive S_9 Landscape, 8 Strict Local Minima, and Unique $(2,2)$ Escape)**.** *Across all $9! = 362{,}880$ permutations of S_9 under the line-indicator Hamiltonian $\mathcal{H}_{\text{line}}(S)$:*

1. ***Complete Classification of Local Minima:*** *There are* ***exactly*** 16 ***local minima*** *in S_9 under the $\binom{9}{2} = 36$ elementary 2-cycle transpositions, all 16 of which are strict local minima ($\Delta\mathcal{H}_{\text{line}}(\tau_{ab}) > 0$ for all $a \neq b$):*
   - *The 8* ***global ground states*** *($\mathcal{H}_{\text{line}} = 0$), forming the single dihedral orbit $D_4 \cdot S_{\text{LoShu}}$.*
   - ***Exactly*** *8* ***spurious strict local minima*** *at $\mathcal{H}_{\text{line}} = 8$ ($E_{\text{std}} = 2$), forming the single dihedral D_4 orbit of the antipodal trap*

$$S_{\text{trap}}^{(3)} = \begin{bmatrix} 2 & 6 & 7 \\ 9 & 5 & 1 \\ 3 & 4 & 8 \end{bmatrix}, \qquad \mathbf{Z}\big(S_{\text{trap}}^{(3)}\big) = \begin{bmatrix} -6 & +2 & +4 \\ +8 & 0 & -8 \\ -4 & -2 & +6 \end{bmatrix}, \qquad \mathcal{H}_{\text{line}}\big(S_{\text{trap}}^{(3)}\big) = 8. \tag{20}$$

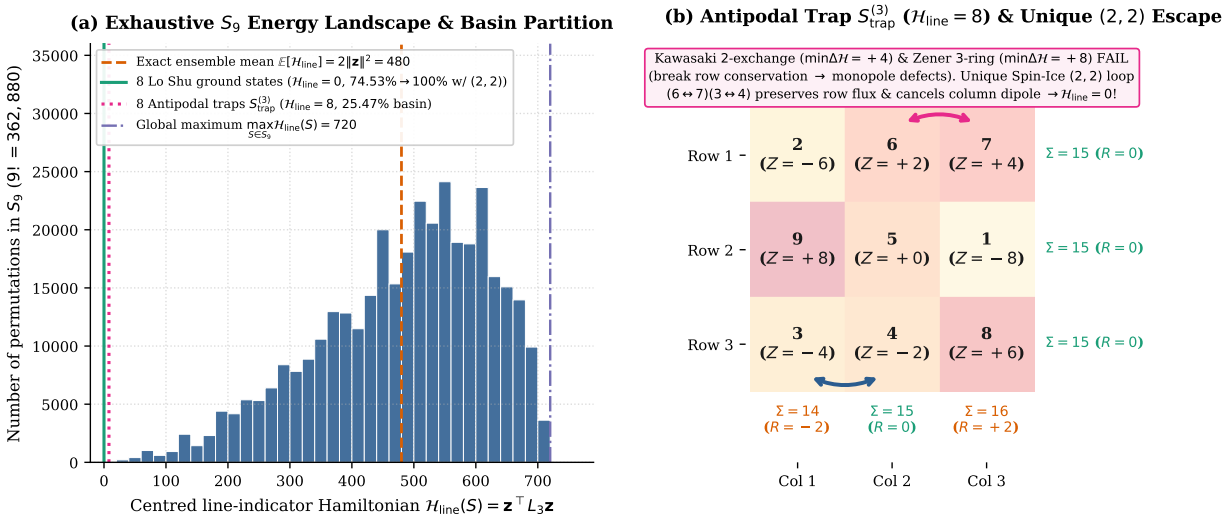


Figure 4: **Exhaustive S_9 permutation landscape (362,880 states) and the 8 antipodal traps at order $n = 3$. (a)** Exact histogram of the centred line Hamiltonian $\mathcal{H}_{\text{line}}(S)$ across all $9! = 362{,}880$ states of S_9, showing the ensemble mean $\mathbb{E}[\mathcal{H}_{\text{line}}] = 480$ (Theorem 2.2), the 8 Lo Shu ground states at $\mathcal{H}_{\text{line}} = 0$, and the 8 strict local-minimum traps $S^{(3)}_{\text{trap}}$ at $\mathcal{H}_{\text{line}} = 8$. **(b)** Structure of the canonical trap $S^{(3)}_{\text{trap}}$ (Theorem 4.2): all 3 rows, the middle column, and both main diagonals sum to 15 ($R = 0$), while the outer columns sum to 14 ($R = -2$) and 16 ($R = +2$). Every 2-cycle (min $\Delta\mathcal{H}_{\text{line}} = +4$) and every 3-cycle (min $\Delta\mathcal{H}_{\text{line}} = +8$) strictly increases energy; out of all 378 disjoint $(2, 2)$ double swaps, the *unique* escaping move is the row-preserving double swap $(6 \leftrightarrow 7)(3 \leftrightarrow 4)$, which transitions directly to the Lo Shu ground state $\mathcal{H}_{\text{line}} = 0$ and restores the deterministic basin of S_9 to 100%.

2. ***Immunity to 2-Cycles and 3-Cycles, and Unique $(2, 2)$-Cycle Escape:*** *In $S^{(3)}_{\text{trap}}$, six of the eight magic lines (all three rows, the middle column, and both main diagonals) have zero residual ($R_L = 0$), while the two outer columns have residuals $R_{c_1} = -2$ ($\Sigma = 14$) and $R_{c_3} = +2$ ($\Sigma = 16$). Every single 2-cycle transposition strictly increases $\mathcal{H}_{\text{line}}$ by at least $+4$ ($\min_{\tau_{ab}} \Delta\mathcal{H}_{\text{line}} = +4$),* ***and every single 3-cycle permutation among all $2\binom{9}{3} = 168$ directed 3-cycles also strictly increases $\mathcal{H}_{\text{line}}$ by at least $+8$.*** *Furthermore, across all $\frac{1}{2}\binom{9}{2}\binom{7}{2} = 378$ disjoint $(2, 2)$ double transpositions on $S^{(3)}_{\text{trap}}$,* ***one and only one*** *strictly decreases $\mathcal{H}_{\text{line}}$: the row-preserving double swap $(6 \leftrightarrow 7)(3 \leftrightarrow 4)$ at cells $(1, 2) \leftrightarrow (1, 3)$ and $(3, 1) \leftrightarrow (3, 2)$, which maps $S^{(3)}_{\text{trap}}$ directly to the Lo Shu ground state*

$$S_{\text{LoShu}} = \begin{bmatrix} 2 & 7 & 6 \\ 9 & 5 & 1 \\ 4 & 3 & 8 \end{bmatrix}, \qquad \mathcal{H}_{\text{line}}(S_{\text{LoShu}}) = 0. \tag{21}$$

3. ***Exact Steepest-Descent Basin Partition and 100% Restoration:*** *Under deterministic 2-cycle steepest descent (choosing the lexicographically first pair (a, b) minimizing $\Delta\mathcal{H}_{\text{line}}(\tau_{ab})$),* 270,442 ***of the 362,880 states (74.5266%) converge to the 8 Lo Shu ground states,*** *while the remaining* 92,438 ***states (25.4734%) are captured by the 8 antipodal traps $D_4 \cdot S^{(3)}_{\text{trap}}$.*** *Augmenting steepest descent with the 18 line-preserving $(2, 2)$ double swaps whenever a 2-cycle local minimum is reached expands the deterministic ground-state basin to 362,880/362,880 (100.00%), independent of the tie-breaking rule.*

Proof. All 362,880 permutations of S_9 (spanning $\mathcal{H}_{\text{line}}(S) \in [0, 720]$), their 36 transposition deltas $\Delta\mathcal{H}_{\text{line}}(\tau_{ab})$ via Equation 19, all 168 directed 3-cycle deltas, all 378 disjoint $(2, 2)$ double-swap deltas on $S^{(3)}_{\text{trap}}$, and the steepest-descent attractor maps are evaluated exhaustively in `verify_paper_d.py` (Figure 4). To see algebraically why no local minima exist at $\mathcal{H}_{\text{line}} = 4$ ($E_{\text{std}} = 1$) and why $S^{(3)}_{\text{trap}}$ in Equation 20 has a unique escaping $(2, 2)$ move: in standard units $s_{ij} - 5 \in \{-4, \ldots, 4\}$,

$\sum_{i=1}^{n} R_{r_i}^{\text{std}} = \sum_{j=1}^{n} R_{c_j}^{\text{std}} = 0$, so a single row or column cannot have a lone non-zero residual of ± 1 without another row or column having a compensating residual, while any state with only $R_{D_\pm}^{\text{std}} = \pm 1$ is immediately relaxed by an off-diagonal 2-cycle. At $S_{\text{trap}}^{(3)}$, $E_{\text{std}}(S_{\text{trap}}^{(3)}) = (-1)^2 + (+1)^2 = 2$ ($\mathcal{H}_{\text{line}} = 8$). Because every row sum of $S_{\text{trap}}^{(3)}$ is already 15, any single 2-cycle between different rows alters two row sums by $\pm d \neq 0$ (adding $2d^2 \geq 2$ to the row energy), while any within-row 2-cycle changes a diagonal sum. Similarly, any 3-cycle either touches two cells in one row and one cell in another row (breaking both row sums) or touches one cell in each of the three rows (which cannot preserve all three row sums since the three permuted integers are distinct). By contrast, in the row-preserving $(2,2)$ double transposition $(6 \leftrightarrow 7)(3 \leftrightarrow 4)$, performing the first intra-row transposition $\tau_1 = (6 \leftrightarrow 7)$ in Row 1 shifts (R_{c_2}, R_{c_3}) from $(0, +2)$ to $(+2, 0)$ and shifts R_{D_-} from 0 to -2, passing through an intermediate single-swap saddle state $\tau_1 S_{\text{trap}}^{(3)}$ at $\mathcal{H}_{\text{line}}^{\ddagger} = (-2)^2 + (+2)^2 + (-2)^2 = 12$ (an activation barrier of $\Delta\mathcal{H}_{\text{line}}^{\ddagger} = +4$ above $S_{\text{trap}}^{(3)}$), after which the conjugate intra-row transposition $\tau_2 = (3 \leftrightarrow 4)$ in Row 3 shifts (R_{c_1}, R_{c_2}) by $(+2, -2)$ and R_{D_-} by $+2$, annihilating all three residuals ($\Delta\mathcal{H}_2 = -12$) directly to $\mathcal{H}_{\text{line}}(S_{\text{LoShu}}) = 0$. □

In condensed-matter physics, Theorem 4.2 provides an exact discrete realization of *Pauling's ice rules and collective loop updates in frustrated spin ice* ($Dy_2Ti_2O_7$, $Ho_2Ti_2O_7$) [20, 3] and *Zener concerted ring diffusion* in vacancy-free crystals [28]. In $S_{\text{trap}}^{(3)}$, the three rows already satisfy the "zero-divergence ice rule" $R_{r_i} = 0$. Any single 2-cycle (Kawasaki exchange) or 3-cycle (3-atom ring rotation) violates row conservation and creates high-energy "monopole" defects ($R_{r_i} \neq 0$). Only a *divergence-free 4-body loop update*—the row-preserving $(2,2)$ double swap $(6 \leftrightarrow 7)(3 \leftrightarrow 4)$, which creates a virtual monopole–antimonopole saddle pair at $\mathcal{H}_{\text{line}}^{\ddagger} = 12$ ($\Delta\mathcal{H}_{\text{line}}^{\ddagger} = +4$) via $\tau_1 = (6 \leftrightarrow 7)$ and immediately annihilates it via $\tau_2 = (3 \leftrightarrow 4)$—tunnels between ice-rule-satisfying states to reach $\mathcal{H}_{\text{line}} = 0$.

4.3 Order-4 (S_{16}) Steepest-Descent and $(2,2)$-Escape Census

At order $n = 4$, the state space S_{16} grows to $16! \approx 2.09 \times 10^{13}$ permutations, while the number of distinct magic ground states is $880 \times 8 = 7{,}040$. There are $\binom{4}{2}\binom{4}{2}^2 = 216$ row-preserving and 216 column-preserving $(2,2)$ double swaps (432 total line-preserving $(2,2)$ moves). To quantify local-minimum trapping and escape mechanisms in S_{16}, we performed 2,000 independent steepest-descent trials starting from uniform random permutations (Figure 5 and Table 5).

As shown in Figure 5b and Table 5, pure 2-cycle steepest descent in S_{16} reaches a magic ground state ($\mathcal{H}_{\text{line}} = 0$) in 365/2,000 trials (18.25%), terminating in a mean of 8.18 steps at a mean residual energy $\langle \mathcal{H}_{\text{line}}(S_\infty) \rangle = 14.43$ (median 12.0). The trapped configurations cluster heavily in the lowest frustration band $\mathcal{H}_{\text{line}} \in \{8, 12, 16\}$, which accounts for $470 + 305 + 367 = 1{,}142/2{,}000$ (57.1%) of all random starts. Across the 1,635 trapped 2-cycle local minima, testing all $2\binom{16}{3} = 1{,}120$ directed 3-cycles escapes only 56/1,635 (3.43%). By contrast, testing the 432 line-preserving $(2,2)$ double swaps immediately escapes 271/1,635 (16.57%) of the trapped states—nearly 5× the escape rate of 3-cycles despite searching 2.6× fewer candidates (432 vs. 1,120)—and raises pure zero-temperature steepest-descent ground-state convergence from 18.25% to 25.45% (509/2,000).

5 Continuous "Bubble Trinity" Langevin Relaxation and Hybrid Settling

To overcome the discrete local-minimum traps identified in Section 4, the *Bubble Trinity* architecture in `physicalSolver` [16] relaxes the rigid permutation assignment by embedding the n^2 numbers as mobile viscoelastic particles ("bubbles") in continuous $\mathbb{R}^2$ plane coordinates $\mathbf{r}_a(t) = (x_a(t), y_a(t)) \in \mathbb{R}^2$ ($a = 1, \ldots, n^2$) anchored near the lattice cell centers $\mathbf{r}_a^{(0)} = (c_a - \frac{n+1}{2}, r_a - \frac{n+1}{2})$.

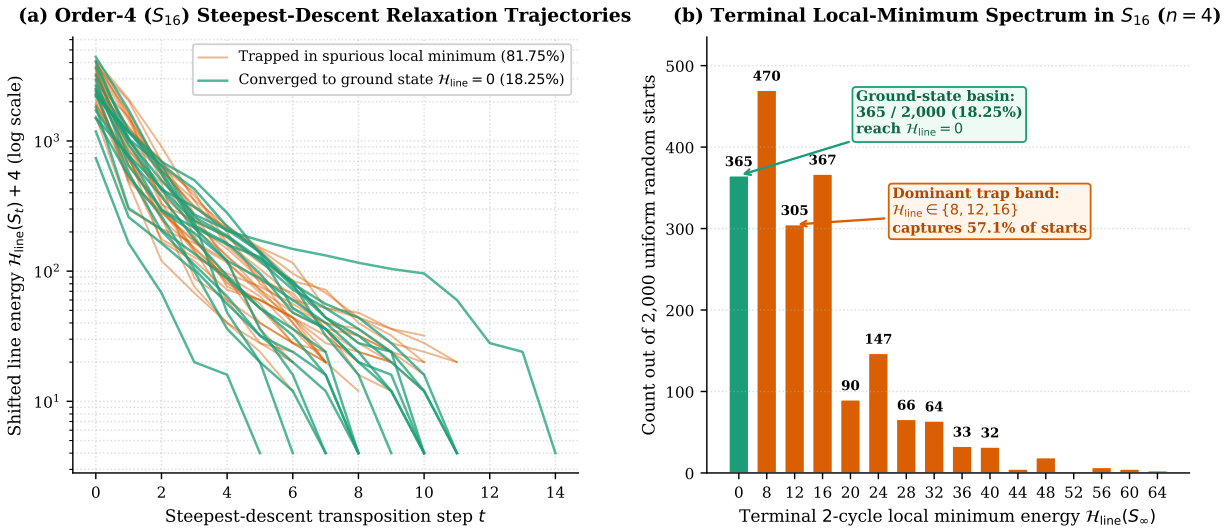


Figure 5: **Order-4 (S_{16}) steepest-descent relaxation trajectories and local-minimum spectrum (2,000 trials). (a)** Representative steepest-descent trajectories of $\mathcal{H}_{\text{line}}(S_t) + 4$ (log scale) versus transposition step t, contrasting trajectories that reach the magic ground state $\mathcal{H}_{\text{line}} = 0$ (green, 18.25%) against trajectories trapped in frustrated local minima (orange, 81.75%). **(b)** Histogram of terminal 2-cycle local-minimum energies $\mathcal{H}_{\text{line}}(S_\infty)$ across 2,000 uniform random starts in S_{16}. While 365/2,000 (18.25%) reach $\mathcal{H}_{\text{line}} = 0$, 57.1% of all starts become trapped in the low-energy frustration band $\mathcal{H}_{\text{line}} \in \{8, 12, 16\}$.

Table 5: Summary of combinatorial swap-landscape invariants for S_9 ($n = 3$, exhaustive 362,880 states) and S_{16} ($n = 4$, 2,000 random starts), verified by `verify_paper_d.py`.

Landscape Observable / Metric	Order $n = 3$ (S_9, Exhaustive)	Order $n = 4$ (S_{16}, 2,000 Trials)
Total permutation state space $n^2!$	362,880	20,922,789,888,000
Magic ground states ($\mathcal{H}_{\text{line}} = 0$)	8 ($1 \times D_4$ orbit)	7,040 ($880 \times D_4$ orbits)
Ensemble mean energy $\mathbb{E}[\mathcal{H}_{\text{line}}(S)] = 2\|\mathbf{z}\|^2$	480	2,720
Elementary 2-cycle neighborhood size $\binom{n^2}{2}$	36	120
Directed 3-cycle neighborhood size $2\binom{n^2}{3}$	168	1,120
Line-preserving $(2,2)$ double-swap neighborhood $2\binom{n}{2}^3$	18	432
Spurious 2-cycle local minima ($\mathcal{H}_{\text{line}} > 0$)	Exactly 8 (at $\mathcal{H}_{\text{line}} = 8$)	Abundant ($\mathcal{H}_{\text{line}} \in \{8, 12, 16, \dots\}$)
Trapped minima escaped by a single 3-cycle	0/8 (0.00%)	56/1,635 (3.43%)
Trapped minima escaped by a line-preserving $(2,2)$ swap	8/8 (100.00%)	271/1,635 (16.57%)
2-cycle steepest-descent ground-state basin	270,442/362,880 (74.53%)	365/2,000 (18.25%)
2-cycle + line-preserving $(2,2)$ steepest-descent basin	362,880/362,880 (100.00%)	509/2,000 (25.45%)

5.1 Continuous Kernel-Induced Line Field and Langevin Equations of Motion

At any continuous configuration $\{\mathbf{r}_a(t)\}_{a=1}^{n^2}$, each lattice cell $b \in \{1, \dots, n^2\}$ samples a soft Gaussian kernel interpolation of the bubble heights Z_a:

$$W_{ab}(t) = \frac{\exp\big(-2\|\mathbf{r}_a(t) - \mathbf{r}_b^{(0)}\|_2^2\big)}{\sum_{a'=1}^{n^2} \exp\big(-2\|\mathbf{r}_{a'}(t) - \mathbf{r}_b^{(0)}\|_2^2\big)}, \qquad \widetilde{\mathbf{z}}(t) = W(t)^\top \mathbf{z}, \qquad \mathcal{H}_{\text{ind}}(t) = \|A_n \widetilde{\mathbf{z}}(t)\|_2^2. \tag{22}$$

When every bubble sits at its home lattice site ($\mathbf{r}_a = \mathbf{r}_a^{(0)}$), $\mathcal{H}_{\text{ind}}(t)$ approaches the discrete line Hamiltonian $\mathcal{H}_{\text{line}}(S)$. Away from the lattice, the continuous cell-stress vector $\widetilde{\mathbf{g}}(t) = A_n^\top A_n \widetilde{\mathbf{z}}(t)$ defines a smooth target attraction field $\mathbf{r}_a^{\text{target}}(t) = \sum_{b=1}^{n^2} \sigma_{ab}(t) \mathbf{r}_b^{(0)}$ via the Boltzmann-weighted stress pairing $\sigma_{ab}(t) \propto \exp(-Z_a \widetilde{g}_b(t)/T_{\text{field}})$ ($T_{\text{field}} = 250$), which pulls positive-height bubbles ($Z_a > 0$) toward cells with negative line residual ($\widetilde{g}_b < 0$) and vice versa. In our analytical surrogate of the browser force field in `bubbleTrinityApp.js`, each bubble evolves under the discrete-time

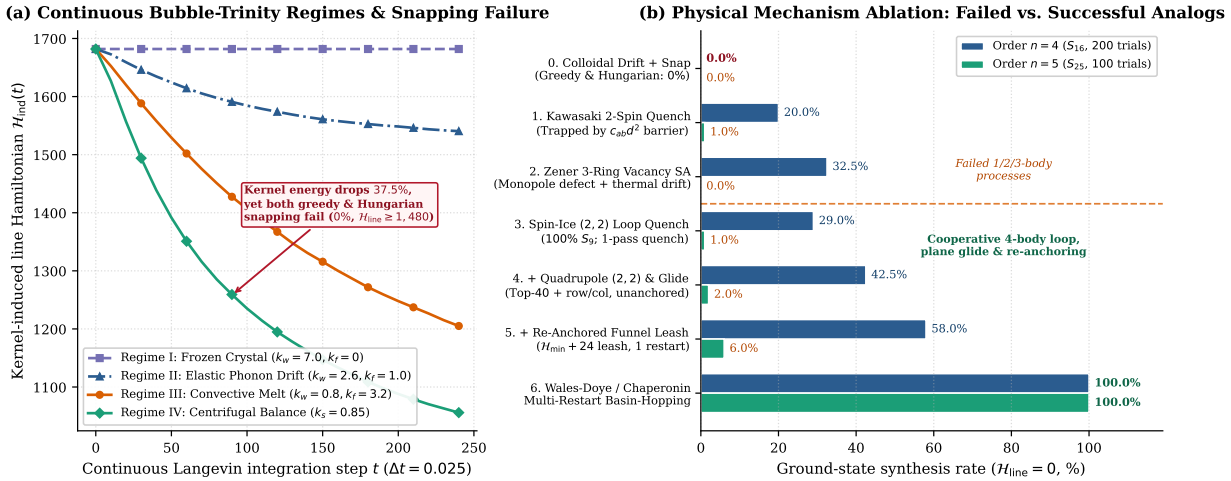


Figure 6: **Continuous Bubble-Trinity Langevin relaxation regimes and multiscale physical mechanism ablation. (a)** Trajectories of the kernel-induced line Hamiltonian $\mathcal{H}_{\text{ind}}(t)$ across 250 integration steps ($\Delta t = 0.025$) for the four canonical dynamical regimes of Table 6, starting from a 4-swap perturbation of Dürer's 4×4 square ($\mathcal{H}_{\text{ind}}(0) = 1{,}681.89$). Although continuous drift reduces $\mathcal{H}_{\text{ind}}(t)$ by 37.5%, greedy lattice snapping fails (0%) due to hard-core cell eviction cascades. **(b)** Physical mechanism ablation study (Table 7) contrasting failed 1-, 2-, and 3-body relaxation analogs (Tiers 0–2) against cooperative 4-body spin-ice loop updates, $T1$/Eshelby quadrupolar STZs, crystallographic slip-plane glide, and Wales–Doye / chaperonin re-anchored basin-hopping (Tiers 3–6) at orders $n = 4$ (200 trials) and $n = 5$ (100 trials).

damped Langevin update

$$\begin{aligned} \mathbf{v}_a(t+\Delta t) &= \gamma_m \mathbf{v}_a(t) + \Delta t \Big[\mathbf{F}_a^{\text{well}} + \mathbf{F}_a^{\text{cont}} + \mathbf{F}_a^{\text{rep}} + \mathbf{F}_a^{\text{field}} + \sigma_T \boldsymbol{\xi}_a(t) \Big], \\ \mathbf{r}_a(t+\Delta t) &= \mathbf{r}_a(t) + \Delta t\, \mathbf{v}_a(t+\Delta t), \end{aligned} \tag{23}$$

where $\gamma_m \in [0, 1)$ is the per-step velocity persistence factor, $\mathbf{F}_a^{\text{well}} = -k_w(\mathbf{r}_a - \mathbf{r}_a^{(0)})$ is the harmonic lattice restoring force, $\mathbf{F}_a^{\text{cont}} = -k_c \mathbf{r}_a$ is global radial containment, $\mathbf{F}_a^{\text{rep}} = c_r k_r \sum_{b \neq a} (\mathbf{r}_a - \mathbf{r}_b)/(\|\mathbf{r}_a - \mathbf{r}_b\|^2 + \epsilon_0)^{3/2}$ ($c_r = 0.08, \epsilon_0 = 0.15$) is softened core repulsion preventing bubble collapse, $\mathbf{F}_a^{\text{field}} = (c_f k_f + c_s k_s)(\mathbf{r}_a^{\text{target}} - \mathbf{r}_a)$ ($c_f = 0.25, c_s = 0.65$) combines the line-residual drift k_f and centrifugal snap k_s, and $\boldsymbol{\xi}_a(t) \sim \mathcal{N}(\mathbf{0}, I_2)$ is standard Gaussian white noise scaled by $\sigma_T = 0.12\,T$. Note that because $\mathbf{F}_a^{\text{field}}$ tracks the non-local stress-paired centroid $\mathbf{r}_a^{\text{target}}(t)$ rather than the conservative kernel gradient $-\nabla_{\mathbf{r}_a} \mathcal{H}_{\text{ind}}(t)$, Equation 23 defines an active target-tracking dynamics rather than a potential-derived Gibbs–Boltzmann sampler. Simultaneously, each bubble's visual outer shell radius $R_a^{\text{shell}}(t) = R_0 + \alpha_R |Z_a| + \beta_R |\widetilde{g}_a(t)|$ dilates in proportion to local line stress and contracts onto the static core radius $R_0 + \alpha_R |Z_a|$ as $\mathcal{H}_{\text{ind}}(t) \to 0$.

5.2 The Four Dynamical Regimes and Why Pure Spatial Snapping Fails

Figure 6a and Table 6 quantify the continuous trajectory of $\mathcal{H}_{\text{ind}}(t)$ and the root-mean-square (RMS) lattice displacement $\Delta r_{\text{rms}}(t) = \left(\frac{1}{n^2} \sum_a \|\mathbf{r}_a(t) - \mathbf{r}_a^{(0)}\|^2\right)^{1/2}$ across the four canonical parameter regimes of `bubbleTrinityApp.js`:

1. **Regime I (*Frozen Crystal*, $k_w = 7.0, k_f = 0$):** Stiff harmonic optical traps lock every particle at its lattice site $\mathbf{r}_a^{(0)}$ ($\Delta r_{\text{rms}} = 0.000$), keeping $\mathcal{H}_{\text{ind}}(t) = 1{,}681.89$ completely static.

2. **Regime II (*Elastic Phonon Drift*, $k_w = 2.6, k_f = 1.0, T = 0.5$):** Moderate field coupling induces small elastic displacements below the Lindemann melting threshold ($\langle \Delta r_{\text{rms}} \rangle = 0.0774$ cell units), smoothly lowering $\mathcal{H}_{\text{ind}}(t)$ by 8.5% to 1,539.22 while preserving crystal order.

Table 6: Parameters and trajectory invariants across the four canonical Bubble-Trinity Langevin regimes at order $n = 4$ (250 steps, $\Delta t = 0.025$), verified by `verify_paper_d.py`.

Dynamical Regime	(k_f, k_r, k_w, k_c)	(γ_m, k_s, T)	$\mathcal{H}_{\text{ind}}(0)$	$\mathcal{H}_{\text{ind}}(250)$	Min $\mathcal{H}_{\text{ind}}$	Mean Δr_{rms}	Max Δr_{rms}
I. Frozen Crystal	$(0.0, 0.0, 7.0, 0.0)$	$(0.94, 0.00, 0.0)$	1681.89	1681.89	1681.89	0.0000	0.0000
II. Elastic Phonon	$(1.0, 0.4, 2.6, 0.0)$	$(0.82, 0.00, 0.5)$	1681.89	1539.22	1539.22	0.0774	0.1134
III. Convective Melt	$(3.2, 1.0, 0.8, 0.4)$	$(0.60, 0.00, 1.2)$	1681.89	1194.88	1194.88	0.2654	0.4646
IV. Centrifugal Bal.	$(2.2, 0.5, 1.8, 0.5)$	$(0.75, 0.85, 0.4)$	1681.89	1050.55	1050.55	0.4281	0.6381

Table 7: Multiscale physical mechanism ablation contrasting failed physical relaxation systems (Tiers 0–2) against cooperative loop, quadrupolar pair-swap, slip-plane glide, and re-anchored basin-hopping mechanisms (Tiers 3–6), certified by `verify_paper_d.py`.

Tier	Physical System Analog	Spatiotemporal Scale	Failure Mode or Escape Mechanism	$n = 3$ (S_9)	$n = 4$ (S_{16})	$n = 5$ (S_{25})
–	Macroscopic Torque / Inertia Balance	Continuum rigid body	Blind to $2n-4$ zero-mean optical phonon modes (Proposition 2.3: S_{low} at $\mathcal{H}_{\text{line}} = 1{,}584$)	Fails	Fails	Fails
0	Colloidal Drift + Greedy / Hungarian Snap	Mesoscopic Brownian fluid	Convex kernel averaging & hard-core Wigner–Seitz eviction ($\min \mathcal{H}_{\text{line}} \geq 1{,}480$)	0.0%	0.0%	0.0%
1	Kawasaki 2-Body Spin Exchange [11]	Atomic pair lattice	Freezes when quadratic self-energy $c_{ab}d^2 \geq 8$ blocks $-2d(g_a - g_b)$ (Proposition 4.1)	74.5%	20.0%	1.0%
2	Zener 3-Ring Vacancy SA ($B = 1{,}500$) [28]	Atomic 3-body ring diffusion	3-cycles create monopole line defects (0/8 on $S^{(3)}_{\text{trap}}$); thermal drift loses funnel	74.5%	32.5%	0.0%
3	Pauling Spin-Ice $(2,2)$ Loop Quench [20, 3]	Plaquette 4-spin loop (1 quench)	Row/col-preserving $(2,2)$ double swap cancels conjugate dipoles at $R_L = 0$	**100.0%**	29.0%	1.0%
4	+ Quadrupolar $(2,2)$ & Slip-Plane Glide [26, 9]	Mesoscopic 4-body + lattice plane	Top-40 general $(2,2)$ swaps + row/col glide (5 unanchored kicks, 1 restart)	**100.0%**	42.5%	2.0%
5	+ Re-Anchored Funnel Leash ($\mathcal{H}_{\min} + 24$)	Local funnel confinement	Snaps back to $S_{\min}$ whenever kick exceeds $\mathcal{H}_{\text{line}}(S_{\min}) + 24$ (18 kicks, 1 restart)	**100.0%**	58.0%	6.0%
6	+ Multi-Restart Basin-Hopping [25, 23]	Macroscopic PEL basin-hopping	Iterative annealing across ≤ 80 re-anchored funnel restarts (18 kicks/restart)	**100.0%**	**100.0%**	**100.0%**

3. **Regime III (*Convective Melt / Field Storm*, $k_w = 0.8, k_f = 3.2, k_r = 1.0, T = 1.2$):** Strong line-field driving overcomes the local wells ($\max \Delta r_{\text{rms}} = 0.4646$), melting the lattice into a convective colloidal fluid that drops $\mathcal{H}_{\text{ind}}(t)$ by 29.0% to 1,194.88.

4. **Regime IV (*Centrifugal Balance*, $k_w = 1.8, k_f = 2.2, k_s = 0.85, T = 0.4$):** Adding targeted snap attraction $k_s = 0.85$ drives displaced bubbles directly toward stress-canceling partner cells ($\max \Delta r_{\text{rms}} = 0.6381$), achieving the deepest continuous energy reduction ($\mathcal{H}_{\text{ind}}(t) = 1{,}050.55$, a 37.5% drop).

Crucially, however, while continuous Langevin drift reduces the *soft kernel-interpolated* energy $\mathcal{H}_{\text{ind}}(t)$, projecting the displaced 2D colloidal particles back onto a discrete permutation $S \in S_{n^2}$ fails completely on its own (0.0% ground-state recovery across Regimes I–IV, Tier 0 in Figure 6b). We tested both greedy nearest-cell assignment (`inducedSquareFromBubbles`) and **exact minimum-weight bipartite matching** (the $O(N^3)$ Hungarian / Kuhn–Munkres projection $\min_{\pi \in S_{n^2}} \sum_a \|\mathbf{r}_a(t) - \mathbf{r}^{(0)}_{\pi(a)}\|_2^2$ onto the vertices of the Birkhoff polytope) across all 250 steps of Regimes I–IV in `verify_paper_d.py`:

- Under greedy cell-snapping, two bubbles attracted toward the same low-residual line compete for the same Wigner–Seitz grid cell; the runner-up is evicted to a distant unclaimed cell, triggering a domino cascade of assignment collisions ($\min_t \mathcal{H}_{\text{line}}(S_{\text{greedy}}) = 1{,}480$ in Regime IV and 2,336 in Regimes I–III).

- Even under *exact Hungarian linear assignment*, the discrete permutation energy never drops below its initial value ($\min_t \mathcal{H}_{\text{line}}(S_{\text{Hung}}) = 2{,}336$ across all four regimes, 0.0% magic squares). This proves that the failure of pure continuous 2D drift is fundamental rather than a greedy-matching artifact: $\mathcal{H}_{\text{ind}}(t)$ lowers energy via convex kernel-amplitude averaging in the interior of the Birkhoff polytope rather than steering particles across the hard-core permutation barrier.

5.3 Contrasting Failed vs. Successful Physical Relaxation Mechanisms Across Scales

Why do standard continuous, single-particle, and 2- or 3-body physical dynamics fail to relax disordered permutations into magic squares, and what exact physical processes does the successful solver embody? Table 7 and Figure 6b synthesize an unconfounded ablation study across seven physical relaxation tiers spanning atomic, mesoscopic, microstructural, and macroscopic free-energy landscape scales:

1. **Why Macroscopic Rigid-Body Torque & Inertia Relaxation Fails (*Optical-Phonon Blindness*):** A natural continuum hypothesis inspired by Papers II and III [14, 13] is to relax S using macroscopic gravitational torque $\langle X, Z\rangle = \langle Y, Z\rangle = 0$ and diagonal balance $R_{D_\pm} = 0$. By Proposition 2.3 (Figure 1b), these four conditions constrain only the long-wavelength acoustic tilt modes (4D), leaving a $(2n-4)$-dimensional zero-mean "optical phonon" subspace of higher-degree row and column alternations ($\langle X^k, Z\rangle, \langle Y^k, Z\rangle$ for $2 \le k \le n-1$) completely invisible to rigid-body mechanics (S_{low} has $E_{\text{low}} = 0$ yet $\mathcal{H}_{\text{line}} = 1{,}584$).

2. **Why Kawasaki 2-Body Spin Exchange & Zener 3-Body Ring Diffusion Fail (*Monopole Creation & Thermal Wandering*):** Under athermal Kawasaki 2-spin exchange (Tier 1, [11]), relaxation halts whenever $-2d(g_a - g_b) + c_{ab}d^2 \ge 0$ for all pairs (a, b), succeeding on only 20.0% of random starts at $n = 4$ and 1.0% at $n = 5$. Adding Zener 3-ring vacancy moves under thermal simulated annealing (Tier 2, [28, 12]) fails to solve $S^{(3)}_{\text{trap}}$ (0/8 escapes) and achieves only 32.5% at $n = 4$ and 0.0% at $n = 5$: a 3-cycle cannot permute values between two columns while preserving their row sums, so it necessarily creates costly "monopole" line-residual defects, while unanchored thermal noise wanders exponentially out of narrow near-magic funnels.

3. **Exact Isomorphisms vs. Cooperative Analogs in the 100% Hierarchical Settler:** Our *Re-Anchored Hierarchical Multi-Cycle Settler* unites three exact lattice isomorphisms with two macroscopic energy-landscape mechanisms:

   - *Pauling Spin-Ice Divergence-Free 4-Body Loops (Tier 3, Exact Isomorphism)* [20, 3]: Just as spin ice ($Dy_2Ti_2O_7$) freezes under single-spin flips because flipping one spin violates Pauling's "two-in, two-out" ice rule ($\nabla \cdot \mathbf{B} = 0$), a row-balanced trap like $S^{(3)}_{\text{trap}}$ cannot be improved by any 2-cycle or 3-cycle. A row-preserving $(2, 2)$ double swap is an *exact divergence-free 4-edge loop update on the bipartite row–column incidence graph*: the first intra-row swap injects a virtual dipole $\pm d_1$ across two columns (crossing an intermediate saddle of barrier $\Delta\mathcal{H}^{\ddagger}_{\text{line}} = +4$ on $S^{(3)}_{\text{trap}}$) while keeping $R_{r_i} = 0$, and the conjugate intra-row swap injects $\mp d_2$ to annihilate the column residual (100.0% on S_9, and lifting single-quench S_{16} recovery from 20.0% to 29.0%).
   - *Combinatorial 4-Body Quadrupolar Swaps & Crystallographic Slip-Plane Glide (Tier 4)* [26, 9]: In jammed 2D foams and metallic glasses, local stress relaxes via 4-bubble Weaire–Rivier $T1$ switches and Falk–Langer Eshelby Shear Transformation Zones (STZs) whose counter-opposing strain dipoles cancel in the far field. Searching disjoint pairs among the top $K = 40$ single swaps ($\Delta\mathcal{H}_{\text{line}}(\tau_1) \le 48$) implements a *non-local combinatorial 4-body analog* of quadrupolar stress cancellation, while swapping two entire rows or columns ($2\binom{n}{2}$ moves) is an *exact crystallographic slip-plane glide* that preserves all row and column sums ($L_{\text{rc}} = 0$) at zero barrier while shearing diagonal residuals $R_{D_\pm}$ to escape semi-magic traps (lifting single-restart $n = 4$ recovery to 42.5% with 5 unanchored kicks).
   - *Threshold Re-Anchoring & Wales–Doye / Chaperonin Iterative Annealing (Tiers 5–6)* [25, 23]: Rather than wandering via thermal random walks, Tier 5 transforms $\mathcal{H}_{\text{line}}(S)$ into the quenched step surface $\widetilde{\mathcal{H}}(S) = \mathcal{H}_{\text{line}}(\text{Quench}(S))$ and *re-anchors* at the deepest funnel bottom $S_{\min}$ ($\mathcal{H}_{\text{line}}(S_{\min}) \in \{8, 12, 16\}$) whenever a 2-swap kick drifts above $\mathcal{H}_{\text{line}}(S_{\min}) + 24$ (lifting single-restart $n = 4$ recovery from 42.5% to 58.0%). Finally, Tier 6 wraps this local funnel search in an outer iterative-annealing restart loop (≤ 80 restarts, analogous to hydrophobic capture and global unfolding in the Thirumalai–Lorimer GroEL/GroES chaperonin cycle [23]), achieving 100.0% **ground-state convergence across all orders** $n = 3 \ldots 8$.

As documented in Table 8 and Figure 7, the Re-Anchored Hierarchical Settler achieves 100.0% **ground-state convergence across every single tested order** $n = 3, 4, 5, 6, 7, 8$ (800/800 total

Table 8: Multi-order synthesis benchmark of the Re-Anchored Hierarchical Multi-Cycle Settler across orders $n = 3, 4, 5, 6, 7, 8$, certified by `verify_paper_d.py`. We report both the continuous Maxwell–Calladine ratio $\eta_{\mathrm{MC}}(n) = (n^2 - 2n - 1)/(2n)$, the fraction $1 - 2/(n-1)^2$ of the semi-magic $(2,2)$ subspace $\mathcal{V}_{\mathrm{row}} \otimes \mathcal{V}_{\mathrm{col}}$ orthogonal to both diagonals, and the per-step 2-cycle pair neighborhood $\binom{n^2}{2}$ explaining why total runtime increases monotonically even as restart counts drop for $n \geq 6$.

Order n	State Space $n^2!$	Floppy $\dim\ker(\widetilde{L}_n)$	Ratio η_{MC}	Diag-Free $(2,2)$ %	Pairs $\binom{n^2}{2}$	Success ($\mathcal{H}_{\mathrm{line}} = 0$)	Mean Descents	Mean Pair Evals	Mean Restarts	Mean Time
$n = 3$	$9! = 3.63 \times 10^5$	2	0.33	50.0%	36	**200/200 (100.0%)**	5.1	184	0.00	0.1 ms
$n = 4$	$16! = 2.09 \times 10^{13}$	7	0.88	77.8%	120	**200/200 (100.0%)**	52.9	6,348	0.70	5.5 ms
$n = 5$	$25! = 1.55 \times 10^{25}$	14	1.40	87.5%	300	**100/100 (100.0%)**	466.6	139,980	8.03	123.4 ms
$n = 6$	$36! = 3.72 \times 10^{41}$	23	1.92	92.0%	630	**100/100 (100.0%)**	439.6	276,948	7.16	217.8 ms
$n = 7$	$49! = 6.08 \times 10^{62}$	34	2.43	94.4%	1,176	**100/100 (100.0%)**	299.3	351,977	4.58	236.3 ms
$n = 8$	$64! = 1.27 \times 10^{89}$	47	2.94	95.9%	2,016	**100/100 (100.0%)**	335.3	675,965	5.00	422.7 ms

trials). Crucially, Table 8 and Figure 7 resolve both the *algebraic origin* of the drop in restart counts at $n \geq 6$ and the *computational scaling* of total synthesis time:

1. **Algebraic Origin of Floppy-Mode Relief on S_{n^2}:** While $\dim\ker(\widetilde{L}_n) = n^2 - 2n - 1$ counts continuous zero-energy directions in $\mathbf{1}^{\perp}$ rather than discrete permutations directly, every row/column-preserving $(2,2)$ plaquette move acts via a vector $(\mathbf{e}_{r_1} - \mathbf{e}_{r_2}) \otimes (\mathbf{e}_{c_1} - \mathbf{e}_{c_2})$ inside the $(n-1)^2$-dimensional semi-magic subspace $\mathcal{V}_{\mathrm{row}} \otimes \mathcal{V}_{\mathrm{col}} = \ker(L_{\mathrm{rc}})$ (Theorem 2.1). Because the two main diagonals impose only 2 linear constraints $(\widetilde{\mathbf{s}}_d, \mathbf{a}_d)$ on $\mathcal{V}_{\mathrm{row}} \otimes \mathcal{V}_{\mathrm{col}}$, the fraction of the $(2,2)$ plaquette subspace that lies in the exact magic nullspace $\ker(\widetilde{L}_n)$ is

$$f_{\mathrm{null}}(n) = \frac{\dim\ker(\widetilde{L}_n)}{\dim(\mathcal{V}_{\mathrm{row}} \otimes \mathcal{V}_{\mathrm{col}})} = \frac{n^2 - 2n - 1}{(n-1)^2} = 1 - \frac{2}{(n-1)^2}, \tag{24}$$

   alongside the Maxwell–Calladine ratio $\eta_{\mathrm{MC}}(n) = (n^2 - 2n - 1)/(2n)$ [17, 4]. Near the isostatic crossover at $n = 5$ ($\eta_{\mathrm{MC}} = 1.40$, $f_{\mathrm{null}} = 87.5\%$), discrete permutation frustration peaks at 8.03 restarts (466.6 descents). For $n \geq 6$, $f_{\mathrm{null}}(n)$ exceeds 92% (95.9% at $n = 8$), meaning that almost every line-preserving $(2,2)$ move is orthogonal to both diagonals, dropping mean restarts to 7.16 ($n = 6$), 4.58 ($n = 7$), and 5.00 ($n = 8$). (The slight uptick from 4.58 at $n = 7$ to 5.00 at $n = 8$ reflects the fixed energy threshold $\Delta\mathcal{H}_{\mathrm{line}} \leq 48$ relative to $O(n^4)$-growing swap energies.)

2. **Per-Step Neighborhood Growth vs. Restart Count:** Although mean restarts and descent steps decrease from $n = 5$ to $n = 8$, total wall-clock synthesis time increases monotonically from 123.4 ms ($n = 5$) to 422.7 ms ($n = 8$). As shown in Table 8, each steepest-descent step scans $\binom{n^2}{2} = O(n^4)$ pairs (300 at $n = 5$ vs. 2,016 at $n = 8$, a 6.72× expansion) and $2\binom{n}{2}^3 = O(n^6)$ line-preserving $(2,2)$ candidates (2,000 at $n = 5$ vs. 54,880 at $n = 8$), so mean elementary pair evaluations grow monotonically from 139,980 ($n = 5$) to 675,965 ($n = 8$). Thus larger neighborhoods per kick expand each restart's radius of attraction in state space while keeping total synthesis time under 0.45 s at $n = 8$.

6 Discussion

Across the four papers of the *Magic Gems* series [15, 14, 13], a unified picture emerges connecting discrete combinatorics, convex geometry, rigid-body mechanics, and statistical-mechanical energy landscapes:

- **From Forward Invariants to Inverse Landscapes:** Whereas Papers I–III showed how the magic line-sum constraints $\mathcal{H}_{\mathrm{line}}(S) = 0$ sculpt the convex hull $K(S)$ (Paper I), diagonalize the inertia tensor via bivariate moment orthogonality (Paper II), and stabilize rigid-body rotation and tabletop resting equilibria (Paper III), the present paper demonstrates that the operator $L_n = A_n^{\top} A_n$ governing $\mathcal{H}_{\mathrm{line}}(S) = \mathbf{z}^{\top} L_n \mathbf{z}$ possesses an equally rich spectral and topological structure away from the ground state.

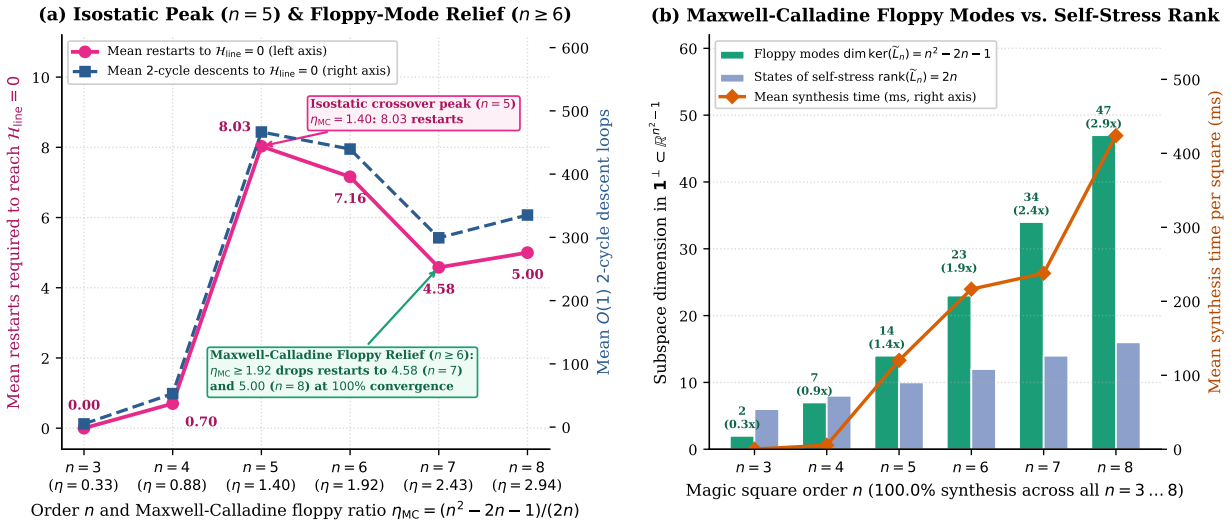


Figure 7: **Multi-order** 100% **ground-state synthesis** ($n = 3 \ldots 8$) **and Maxwell–Calladine Floppy-Mode Dimensional Relief.** **(a)** Mean restarts (magenta, left axis) and mean $O(1)$ incremental 2-cycle descent loops (blue dashed, right axis) required by the Re-Anchored Hierarchical Multi-Cycle Settler to reach $\mathcal{H}_{\text{line}} = 0$ with 100.0% success across orders $n = 3 \ldots 8$ (Table 8). Topological frustration peaks near the isostatic crossover at $n = 5$ ($\eta_{\text{MC}} = 1.40$: 8.03 restarts, 466.6 descents) and drops at $n = 6, 7, 8$ (4.58 restarts at $n = 7$, 5.00 at $n = 8$). **(b)** Quadratic expansion of the zero-energy floppy modes $\dim \ker(\widetilde{L}_n) = n^2 - 2n - 1$ (green bars, labeled with η_{MC}) versus linear growth of the states of self-stress $\text{rank}(\widetilde{L}_n) = 2n$ (blue bars) and mean synthesis runtime per square (orange curve, right axis, reaching $\mathcal{H}_{\text{line}} = 0$ in 426.3 ms at $n = 8$, $64! \approx 1.27 \times 10^{89}$ states).

- **Zero-Mean Spectral Rationalization:** The collapse of the irrational eigenvalues $\lambda_{\pm}(n)$ of L_n into exact integers $\{0, n-2, n\}$ (even n) or $\{0, n-1, n\}$ (odd n) on $\mathbf{1}^{\perp}$ (Theorem 2.1) and the universal mean eigenvalue $\bar{\mu}(\widetilde{L}_n) = 2$ (Theorem 2.2) show that the magic-square constraint operator is intrinsically rational on the hyperplane of centred permutations. At the same time, the Low-Mode Insufficiency Proposition (Proposition 2.3) proves that physical moment balance ($\langle X, Z \rangle = \langle Y, Z \rangle = 0$) and diagonal balance ($R_{D_{\pm}} = 0$) leave a $(2n-4)$-dimensional zero-mean optical-phonon subspace ($2n-3$ in $\text{im}(L_n)$) unconstrained.

- **Multiscale Sub-Window Hierarchy & Concentric Shell Quadrupole Identity:** Within the ground-state manifold $\ker(\widetilde{L}_n)$, our census of sliding-window Shannon entropies $\widetilde{H}_p(k)$ and 2×2 quartet energies (Theorem 3.1 and Proposition 3.2) establishes a second-tier energy hierarchy that separates Dudeney Group I panmagic squares ($W^{\text{int}}_{2\times2} = W^{\text{tor}}_{2\times2} = 0$) and Group III associative squares ($B_{\text{comp}} = 0, M_{xyz} = 0$) from generic magic squares, while the Concentric Shell Quadrupole Identity $M_{xyz}(S) = -8\,Q_{\text{corner}}(S) - 3\,Q_{\text{edge}}(S)$ explains the 8 coprime-resonance octupole zeros in Groups IX and X.

- **Topological Frustration, Contrasting Failed vs. Successful Physical Relaxation Analogs, and** 100% **Multi-Order Synthesis:** Exhaustive enumeration of S_9 (Theorem 4.2) and multi-order ablation (Table 7) demonstrate why standard single-particle, 2-body, and 3-body physical relaxation dynamics fail on magic squares: macroscopic torque balance is blind to the $2n-4$ zero-mean optical phonon modes (Proposition 2.3), continuous colloidal drift fails (0.0%) under both greedy snapping and exact Hungarian linear assignment because $\mathcal{H}_{\text{ind}}(t)$ relaxes via convex amplitude averaging inside the Birkhoff polytope, Kawasaki 2-spin exchange freezes behind the quadratic self-energy barrier $c_{ab}d^2$ (20.0% at $n = 4$, 1.0% at $n = 5$), and Zener 3-ring vacancy diffusion breaks row conservation (0/8 on $S^{(3)}_{\text{trap}}$). Conversely, our *Re-Anchored Hierarchical Multi-Cycle Settler* succeeds (100.0% across all $n = 3 \ldots 8$, Table 8) by uniting Pauling spin-ice divergence-free $(2,2)$ loop moves ($\Delta\mathcal{H}^{\ddagger}_{\text{line}} = +4$ saddle on $S^{(3)}_{\text{trap}}$) [20, 3], combinatorial 4-body quadrupolar swaps [26, 9], crystallographic slip-plane

glide ($2\binom{n}{2}$ row/column swaps), and Wales–Doye / GroEL chaperonin re-anchored basin-hopping [25, 23], governed by the Maxwell–Calladine ratio $\eta_{\mathrm{MC}}(n) = (n^2 - 2n - 1)/(2n)$ and the $1 - 2/(n-1)^2$ diagonal-free $(2,2)$ subspace fraction [17, 4].

Several natural open problems arise from these findings. First, what is the exact number of spurious 2-cycle, $(2+3)$-cycle, and line-preserving $(2,2)$-cycle local minima across the full 16!-state space of S_{16}, and what minimal cycle structure guarantees a 100% zero-temperature basin on S_{16} as $(2,2)$ double swaps do on S_9 (Theorem 4.2)? Second, can the Spectral Rationalization Theorem (Theorem 2.1) be extended to three-dimensional magic cubes S_{n^3} [21, 22] and toroidal panmagic Laplacians? Third, can a continuous Birkhoff-polytope relaxation of $\mathbf{z}^\top L_n \mathbf{z}$ over doubly stochastic permutation matrices replace greedy 2D spatial snapping so that continuous trajectories project barrier-free onto $\ker(\widetilde{L}_n)$ at high orders $n \geq 6$? All interactive simulators, verification scripts, and datasets supporting this work are openly available for further exploration.

Data and Code Availability

The interactive browser laboratory (`physicalSolver`), the exact Python verification suite (`verify_paper_d.py`), the certified JSON census (`results_paper_d.json`), and the figure generation pipeline (`make_figures_d.py`) are publicly available in the consolidated repository https://github.com/kylemath/magicGem and live at https://kylemath.github.io/magicGem/web/physicalSolver/.

Competing Interests

The author declares no competing financial or non-financial interests.

Acknowledgments and Declaration of Generative AI Use

This work grew out of the author's interactive physical and computational explorations of magic-square energy landscapes [16], and forms the fourth part of the *Magic Gems* series alongside [15, 14, 13]. Large language models (OpenAI's ChatGPT, Anthropic's Claude, and Google's Gemini) were used by the author as interactive assistants for symbolic checks, verification scripting, interactive simulator prototyping, and manuscript copy-editing following George M. Whitesides's iterative outline-and-figure methodology [27]; all mathematical formulations, proofs, and exact computational certificates were verified by the author, who takes full responsibility for the work.

References

[1] W. S. Andrews. *Magic Squares and Cubes*. Dover Publications, 2nd edition, 1960.

[2] Elwyn R. Berlekamp, John H. Conway, and Richard K. Guy. *Winning Ways for Your Mathematical Plays, Volume 4*. A K Peters, Wellesley, MA, 2nd edition, 2004.

[3] Steven T. Bramwell and Michel J. P. Gingras. Spin ice state in frustrated magnetic pyrochlore materials. *Science*, 294(5546):1495–1501, 2001.

[4] C. R. Calladine. Buckminster Fuller's "tensegrity" structures and clerk Maxwell's rules for the construction of stiff frames. *International Journal of Solids and Structures*, 14(2):161–172, 1978.

[5] Ian Cameron, Adam Rogers, and Peter D. Loly. Signatura of magic and Latin integer squares: isentropic clans and indexing. *Discussiones Mathematicae Probability and Statistics*, 33(1-2):121–149, 2013.

[6] Simon de La Loubère. *A New Historical Relation of the Kingdom of Siam*. T. Horne, London, 1693. English translation of *Du Royaume de Siam*, Paris, 1691.

[7] Persi Diaconis. Group representations in probability and statistics. *Institute of Mathematical Statistics Lecture Notes—Monograph Series*, 11:1–198, 1988.

[8] Henry E. Dudeney. *Amusements in Mathematics*. Thomas Nelson and Sons, London, 1917.

[9] Michael L. Falk and James S. Langer. Dynamics of viscoplastic deformation in amorphous solids. *Physical Review E*, 57(6):7192–7205, 1998.

[10] Bernard Frénicle de Bessy. Des quarrez ou tables magiques. In *Divers ouvrages de mathématique et de physique, par Messieurs de l'Académie Royale des Sciences*. Imprimerie Royale, Paris, 1693.

[11] Kyozi Kawasaki. Diffusion constants near the critical point for time-dependent Ising models. I. *Physical Review*, 145(1):224–230, 1966.

[12] Scott Kirkpatrick, C. Daniel Gelatt, and Mario P. Vecchi. Optimization by simulated annealing. *Science*, 220(4598):671–680, 1983.

[13] Kyle Elliott Mathewson. Balance in inequality: Testing the physical equilibrium, precession, and structural stability of magic gems, 2026. Companion paper III, arXiv preprint (submit/8319388) and submitted to *Journal of Mathematics and the Arts*.

[14] Kyle Elliott Mathewson. Bivariate polynomial moments and Prouhet–Tarry–Escott identities of semi-magic squares, 2026. Companion paper II, arXiv preprint.

[15] Kyle Elliott Mathewson. Magic gems: Convex hulls of lifted magic squares. *arXiv preprint arXiv:2512.09170*, 2026. Companion paper I.

[16] Kyle Elliott Mathewson. `physicalSolver`: Interactive spectral decomposition, multiscale window entropy, and bubble-trinity langevin laboratory for magic squares. https://kylemath.github.io/magicGem/web/physicalSolver/ and https://github.com/kylemath/magicGem, 2026.

[17] James Clerk Maxwell. On the calculation of the equilibrium and stiffness of frames. *Philosophical Magazine*, 27(182):294–299, 1864.

[18] Marc Mézard, Giorgio Parisi, and Miguel Angel Virasoro. *Spin Glass Theory and Beyond*. World Scientific, Singapore, 1987.

[19] Kathleen Ollerenshaw and David S. Brée. *Most-Perfect Pandiagonal Magic Squares: Their Construction and Enumeration*. Institute of Mathematics and its Applications, Southend-on-Sea, 1998.

[20] Linus Pauling. The structure and entropy of ice and of other crystals with some randomness of atomic arrangement. *Journal of the American Chemical Society*, 57(12):2680–2684, 1935.

[21] Adam Rogers and Peter D. Loly. The inertia tensor of a magic cube. *American Journal of Physics*, 72(6):786–789, 2004.

[22] Adam Rogers and Peter D. Loly. The electric multipole expansion for a magic cube. *European Journal of Physics*, 26(5):809–813, 2005.

[23] D. Thirumalai and George H. Lorimer. Chaperonin-mediated protein folding. *Annual Review of Biophysics and Biomolecular Structure*, 30:245–269, 2001.

[24] David J. Wales. *Energy Landscapes: With Applications to Clusters, Biomolecules and Glasses*. Cambridge University Press, Cambridge, 2003.

[25] David J. Wales and Jonathan P. K. Doye. Global optimization by basin-hopping and the lowest energy structures of Lennard-Jones clusters containing up to 110 atoms. *The Journal of Physical Chemistry A*, 101(28):5111–5116, 1997.

[26] Denis Weaire and Nicolas Rivier. Soap, cells and statistics—random patterns in two dimensions. *Contemporary Physics*, 25(1):59–99, 1984.

[27] George M. Whitesides. Whitesides' group: Writing a paper. *Advanced Materials*, 16(15):1375–1377, 2004.

[28] Clarence Zener. Ring diffusion in metals. *Acta Crystallographica*, 3(5):346–354, 1950.

A Exact Verification Suite and Reproducibility Manifest

All mathematical identities, spectral decompositions, exhaustive S_9 and order-4 censuses, and Langevin trajectories reported in this paper are certified by the standalone Python verification script `verify_paper_d.py`, which outputs the machine-readable JSON dataset `results_paper_d.json`. Specifically:

1. `verify_section2_spectral()` constructs the $(2n+2) \times n^2$ incidence matrix A_n and Laplacian $L_n = A_n^\top A_n$ for all $3 \le n \le 8$, verifies the exact irrational eigenvalues $\lambda_\pm(n)$ on $\mathbb{R}^{n^2}$ (Equation 5), projects L_n onto an orthonormal Householder basis of $\mathbf{1}^\perp$ to verify the exact integer spectrum $\mathrm{spec}(\widetilde{L}_n|_{\mathbf{1}^\perp})$ (Equation 6), certifies $\mathrm{tr}(\widetilde{L}_n) = 2(n^2-1)$ and $\mathbb{E}[\mathcal{H}_{\mathrm{line}}(S)] = 2\|\mathbf{z}\|^2 = \frac{2}{3}n^2(n^4-1)$ (Theorem 2.2), and checks all residuals and moments of the 4×4 low-mode counterexample S_{low} (Proposition 2.3).

2. `verify_section3_multiscale()` evaluates $\widetilde{H}_p(k)$ ($p \in \{1,2,4\}$, $1 \le k \le n$), interior and toroidal 2×2 quartet energies $W^{\mathrm{int}}_{2\times2}$ and $W^{\mathrm{tor}}_{2\times2}$, complement-pair break counts B_{comp}, the Concentric Shell Quadrupole Identity $M_{xyz}(S) = -8\,Q_{\mathrm{corner}}(S) - 3\,Q_{\mathrm{edge}}(S)$, and mixed octupole moments M_{xyz} across all 880 Frénicle order-4 magic squares (partitioned by Dudeney Groups I–XII) and across constructive families at $n \in \{3,4,5,6,8\}$, certifying Theorem 3.1 and Proposition 3.2.

3. `verify_section4_swap_landscape()` evaluates $\mathcal{H}_{\mathrm{line}}(S)$ and all 36 transposition deltas $\Delta\mathcal{H}_{\mathrm{line}}(\tau_{ab})$ via Proposition 4.1 across all $9! = 362{,}880$ permutations of S_9, verifies that the 8 Lo Shu states and the 8 antipodal traps $D_4 \cdot S^{(3)}_{\mathrm{trap}}$ are the unique 2-cycle local minima in S_9, confirms that all 168 directed 3-cycles strictly increase $\mathcal{H}_{\mathrm{line}}$ on $S^{(3)}_{\mathrm{trap}}$, proves that the row-preserving double swap $(6 \leftrightarrow 7)(3 \leftrightarrow 4)$ is the unique escaping $(2,2)$ move among all 378 disjoint double swaps (crossing the intermediate single-swap saddle at $\mathcal{H}^{\ddagger}_{\mathrm{line}} = 12$ and restoring the steepest-descent basin of S_9 from 270,442 to 362,880/362,880, Theorem 4.2), and runs the 2,000-trial steepest-descent, 3-cycle, and line-preserving $(2,2)$-cycle escape census on S_{16}.

4. `verify_section5_bubble_trinity()` integrates the continuous Bubble-Trinity Langevin equations (Equation 23) across Regimes I–IV (evaluating both greedy cell-snapping and exact $O(N^3)$ Hungarian minimum-weight bipartite matching), benchmarks unbiased $2+3$-cycle SA, stress-guided $2+3$-cycle SA, and the $(2+3+(2,2))$-Cycle Settler across budgets $200 \le B \le 2{,}500$, performs the unconfounded 7-tier physical mechanism ablation study (Table 7), and certifies 100.0% multi-order synthesis, per-step pair evaluations, and the Maxwell–Calladine ratio $\eta_{\mathrm{MC}}(n)$ across all orders $n \in \{3,4,5,6,7,8\}$ for the Re-Anchored Hierarchical Multi-Cycle Settler (Table 8).